The Viability of Maximizing Thrust in Hall-Effect Thrusters

A project presented to
The Faculty of the Department of Aerospace Engineering
San José State University

in partial fulfillment of the requirements for the degree
Master of Science in Aerospace Engineering

by

Nader Ali

December 2021

Approved by

Dr. Periklis Papadopoulos
Faculty Advisor

ABSTRACT

The Viability of Maximizing Thrust in Hall-Effect Thrusters

By Nader Ali

Hall-Effect thrusters (HET) are highly promising electric propulsion systems. When properly optimized, they can be effectively utilized in multitudes of different applications. Some of the areas prime for optimization are the geometric parameters and the electric and magnetic circuits. Combined, effective optimization in those areas can produce a system that can fulfill a wide variety of missions. The goal of this work is to present an optimized system that is magnetically shielded to extend the service life, minimize the magnetic circuit mass, and produce an optimal electromagnetic field, all of which help in improving thrust at a given thruster power class. This optimization process is performed using a modified version of the non-dominating sorting genetic algorithm (NSGA-II) inside MATLAB, along with COMSOL Multiphysics. Using a multi-step process, the optimal mass of the circuit along with the dimensions of the thruster channel as well the magnetic field topology are then presented.

ACKNOWLEDGEMENTS

First and foremost, I'd like to offer my sincerest gratitude to Dr. Periklis Papadopoulos for his guidance on not only this project, but for being one of the greatest and kindest teachers I've ever had throughout my attendance at San Jose State University. I'd also like to extend my thanks to Dr. Nikos Mourtos for always being available when his help was needed. Finally, I'd like to thank my parents for never giving up on me.

TABLE OF CONTENTS

LIST OF TABLES

LIST OF FIGURES

NOMENCLATURE

$\dot{m}_p$	Gas flow
$\dot{m}_a$	Anode flow rate
$\dot{m}_c$	Cathode flow rate
η_c	Cathode efficiency
P_{in}	Total power into thruster
P_d	Discharge power
P_k	Cathode keeper power
P_{mag}	Magnetic field power
η_o	Electrical utilization efficiency
P_T	Total power into thruster
P_w	Power into wall
P_{ion}	Ion power
I_{iw}	Ion current to wall
M	Ion mass
m	Mass
ϕ	Potential
ε	Energy
v_{ex}	Exhaust velocity
P_{jet}	Jet power
v_i	Ion velocity
I_b	Beam current
v_b	Beam velocity
g	Gravitational constant
η_m	Mass utilization efficiency
B_z	Magnetic field axial component
D	Cathode housing diameter
L	Channel length
I	Coil current
N_o	Outer coil cable turns
w_o	Outer coil thickness
x	Pole gap
B_r	Magnetic field radial component
B_{peak}	Required magnetic field magnitude
B_{sat}	Saturation threshold

Chapter 1 - Introduction

1.1 Motivation

1.1.1 Problem and Reason for Pursuit

Chemical propulsion has been the main driver for both terrestrial and interplanetary exploration. Its long, proven track record is a testament that it works. It does not, however, come without major drawbacks. Not only is chemical propulsion notoriously inefficient, but the fuel it uses is heavy, requires a massive volume of space, is highly volatile and has much lower specific impulse when compared to other forms of propulsion such as electric.

With today's new age of planetary exploration, the need for more efficient, faster, and relatively cheaper propulsion systems has become more essential than ever. This will be even more paramount as the scope of planetary exploration increases in the coming decades.

Currently, chemical propulsion is, and will be the best option to break free of Earth's gravity for the foreseeable future. Once free of gravity, other propulsion options make more sense than chemical options. This is where electric propulsion can be utilized.

Although highly efficient and require less fuel volume space, the pressing problem with electric propulsion systems, specifically hall-effect thrusters in their current state, is their poor thrust-to-weight ratio performance. This is attributed to multiple factors. First, there is a limit to the amount of current supplied to the system before components begin to experience adverse performance effects [1]. Second, plasma-wall interaction proves to be a challenge to electron emission efficiency. Finally, magnetic field instability plays a major role in thrust reduction [1]. The aforementioned factors could be mitigated by optimizing the system, specifically the electromagnetic circuit, which this paper aims to accomplish.

1.1.2 The Interest

Interest in this project stems from the belief that electric propulsion should play a much greater role than it currently does in space exploration, as well as the belief that hall-effect thrusters specifically have a vast untapped potential for improvement that are yet to be explored.

1.2 Literature Review

There exists an extensive library of research on electric propulsion dating back to the 1960s. Though well-understood since the early 1960s, research into hall-effect propulsion specifically, however, has not been as aggressive until very recently. This recent increase in interest in this field has yielded a plethora of high-quality research in various forms.

The following literature review examines the state of hall-effect propulsion today, its benefits, as well as parameter improvements that are claimed by the respective authors to enhance the overall performance of today's hall-effect thrusters.

1.2.1 New Electrical Power Supply System for All-Electric Propulsion Spacecraft

In their paper, authors Ming Fu, Donlai Zhang, and Tiecai Li propose a new power supply system architecture for high-power electric propulsion with the ability to power both the thrusters and the onboard payload. Their interest in conducting this study stems from their claimed disadvantages of traditional centralized power distribution, which they summarize as follows:

- Because the onboard payload is being powered by a centralized power bus, there's a higher probability of inner disturbances, which can cause voltage oscillation that may lead to stability and reliability concerns.
- Traditional power supply, according to the authors, is of low efficiency and produces a wide thermal loss margin because of the power conversions normally employed from solar arrays to the propulsion and onboard systems. This also leads to the need for heatsinks large enough to dissipate the heat, leading to added unnecessary weight and cost to the spacecraft.

- The redundant nature of solar arrays, which is claimed that although redundancy is necessary because it addresses the decrease in their performance due to aging and malfunction, it nonetheless adds more complexity, cost, and weight.

The proposed power distribution architecture is claimed to solve the aforementioned disadvantages by introducing two types of buses. One for directly powering the thrusters, and the other being a high voltage bus (HV) powering the onboard systems. The way it is proposed to work is through the redirection of power from the solar arrays to the two busses and introducing maximum power tracking, which would optimize the performance of the solar arrays and negate the need for redundancies [2].

1.2.2 Long Duration Wear Test Of The NASA HERMeS Hall Thruster

This study presents the results of a 1715-hour long wear test of NASA's magnetically-shielded HERMeS hall-effect thruster to identify any occurring erosion or failure. The purpose of the test is to expose any faults in the thruster design, if any, and to correct them before flight approval [3]. The results gathered are as follows:

- Erosion in the outer and inner front pole cover of the thruster varied by 76 to 300 percent, depending on the discharge voltage.
- Changes in magnetic field strength caused a 40% erosion to the outer and inner front pole cover.
- Changing placement of the cathode to an upstream position relative to pole covers caused an 84% erosion decrease.

1.2.3 Effects Of The Peak Magnetic Field Position On Hall Thruster Discharge Characteristics

This paper explores the effect an optimized magnetic field has on the overall performance of a hall-effect thruster. In the paper, the authors test several magnetic field positions within a hall-effect thruster discharge channel using both plasma diagnostics as well as computational fluid simulations. Their findings show that the change in peak magnetic field position causes the following:

- It directly impacts the location of the zone of ionization.
- It affects the propellant ionization process in terms of ion and electron acceleration and conduction, respectively.

In addition to the aforementioned findings, it was also found that when the peak magnetic field is manipulated such that the ionization occurs in the upstream region of the channel, the rate of ionization and the density of the propellant both increase. This increase in density improves the relative performance, but the increased distance between the ionization location and the channel exit does have one drawback: It reduces the ion current because of the loss of ions to the chamber walls.

The authors finally conclude that the best discharge performance occurs when the peak magnetic field is positioned near the channel outlet. This significantly reduces ion losses to the channel walls as well as plume divergence [4].

1.2.4 Influence Of Hollow Anode Position On The Performance Of A Hall-Effect Thruster With Double-Peak Magnetic Field

This study investigates the performance of a symmetrical double-peak magnetic field in a hall-effect thruster. It focuses on the performance characteristics and the laws that govern a U-shaped hollow anode at varying distances from the magnetic separatrix, in addition to the changes that occur to the discharge with every varying distance. At the end of the study, the authors concluded their findings as follows:

- The length of the anode is directly proportional to the location of the ionization and acceleration regions. In essence, the longer the anode tube is, the further down the channel outlet do the ionization and acceleration regions move.
- The performance took a massive hit when the front end of the anode was placed at the inner separatrix, even with the increased ionization density.
- Best thruster performance was achieved when the front end of the anode was between the inner and outer magnetic separatrices.

The authors go on to explain that the longer the distance from the ionization zone to the outlet, the lesser is the overall performance achieved. This is because the channel walls tend to attract ions, significantly decreasing efficiency as mentioned in a preceding study [5].

1.2.5 Effects Of Channel Wall Material On Thrust Performance And Plasma Characteristics Of Hall-Effect Thrusters

This paper attempts to study whether channel wall material affects the performance of a hall-effect thruster and its plasma characteristics. The authors use three types of materials: Boron nitride (BN), boron nitride-silicon nitride mixture (BNSiN), and boron nitride-aluminum nitride mixture (BNA1N). The study concludes that the performance of the thruster is indeed affected by the choice of channel wall material used and offers the following considerations:

- When boron nitride was used, the highest thrust efficiency was achieved regardless of the magnetic field strengths and discharge voltages used.
- An axial position of the ionization region showed significant change with the change in the materials.
- Current density appeared to be highest when BNA1N was used, and lowest when BN was used.

It is finally concluded that the choice of channel wall material alone isn't enough to produce optimal performance; it needs to be matched with a preferable magnetic field structure to ensure maximum efficiency [6].

1.2.6 Performance Tests Of The Institute Of Plasma Physics And Lase Microfusion's Krypton Hall Thruster

This study aims to investigate the performance differences when using krypton in place of xenon as the propellant in a 500-Watt-class hall-effect thruster. According to the authors, the inexpensive nature of krypton can be an attractive alternative to xenon. During the testing phase, all parameters were kept as constant as possible, particularly the magnetic field topology. At the conclusion of the study, the following results were observed [7]:

- Equally stable thruster operation with very similar thrust and specific impulse was achieved for both propellants.
- Both propellants produced a maximum thrust of about 17mN and a mass flow rate of about 1.17 mg/s.
- Xenon was observed to have a 10% better anode efficiency than krypton.

1.2.7 Investigation Of The Effect Of Hollow Cathode Neutralizer Location On Hall Effect Thruster Efficiency

The authors of this study attempt to investigate the relationship between the position of the hollow cathode neutralizer within a hall-effect thruster and the overall efficiency, while maintaining that thruster efficiency is increased with the decrease of cathode coupling voltage. Additionally, they investigate the effects of the cathode mass flow rate and the current on coupling voltage. Their findings are summarized in the following points [8]:

- Cathode coupling voltage is directly affected by the location of the neutralizer.
- Cathode coupling voltage is inversely proportional to the overall efficiency of the thruster.
- Reduction in coupling voltage could be achieved by decreasing the cathode mass flow rate.

1.2.8 Discharge Characteristics Of A Kilowatt Hall-Effect Thruster With A Variable Channel

A kilowatt hall-effect thruster with inner divergent annular and cylindrical segments near the exit is proposed. A comparison experiment of the discharge is conducted by the authors of this study, with one dataset collected when the propellant is supplied along an axial direction, while the other dataset is of the changes in discharge when the propellant is supplied through the channel centerline. The authors present their results as follows: When the gas is supplied along the channel centerline, propellant and current utilization are both higher, a decrease in the divergence angle of the plume occurs and the overall thrust and anode efficiency improve. These improvements are attributed by the authors to the changes in the ionization and acceleration characteristics caused by the differing supply directions.

It is claimed by the authors that this change in gas supply direction from the axial direction, which is widely used in most hall-effect thrusters, to a channel centerline supply direction yielded an increase in power density by a factor of two, as well as greatly improved thrust [9].

1.2.9 Performance And Plume Evolutions During The Lifetime Test Of A Hall-Effect Thruster

This paper investigates the effects and degradation experienced by a hall-effect thruster during 8000 hours of operation, with a special focus on the changes in performance parameters and plume plasma properties [10]. The set of instrumentation used to gather the data includes:

- An optical imaging system for observing erosion around the insulator rings.
- A set of far-field diagnostic instruments to measure plasma potential, density, ion current density, and energy.

After the study, the authors present the following findings:

- During the first 2000 hours of operation, thrust increases then decreases.
- After 2000 hours until the 8000-hour mark, the thrust value shows an upward trend, stylizing at the very end of the runtime.
- The plume produced exhibits expansion characteristics from around the 1000-hour mark to the 4000-hour mark, while exhibiting contraction from the 4000-hour mark to the 8000-hour mark. This is due to the erosion of the ceramic walls that occurs over time.

1.2.10 Parametric Study Of Two Stable Forms Of Discharge Burning In A Hall-Effect Thruster

This paper studies the changes in operational parameters of a hall-effect thruster that uses two stable, but differing anode efficiencies. The study used a thruster with a discharge diameter of 77 mm and voltage in the range of 500-900 V with a mass flow rate that ranged from two to five mg/s. The main result of this study is concluded that when the anode with the suboptimal efficiency is used, the discharge current increases by 10-30%, while simultaneously a decrease of 5-15% in thrust is produced [11].

1.2.11 Power Processing Unit For Hall-Effect Thrusters On Meteor-M №3 Spacecraft”

This paper explores the development results of the power processing unit of the hall-effect thrusters on the Russian Meteor-M №3 spacecraft. The authors present a detailed analysis of the performance and technical characteristics of the thrusters and compare them to their European counterparts. The study concludes that based on the circuit switching cathodes and monoblock design, the Russian PPU-M class of thrusters are superior to their European counterpart [12].

1.2.12 Computational Model Of A Hall Thruster

According to the authors of this study, using computational modeling to model electron mobility within a hall-effect thruster is extremely difficult; therefore, a hybrid PIC-MCC model was used to achieve the best possible results. The PIC model is based on Bohm diffusion, while the MCC model is based on electron-wall collisions. The results of the study are summed in the following points:

- The Bohm PIC model provided the most optimal performance data and met or exceeded the experimental results.
- The MCC model’s mean potential gradient data proved to be slightly steeper, with a negligible error margin.

Based on the results of both models, the authors conclude that neither of the models provided a preferential solution than the other [13].

1.2.13 Hall Thruster With Grooved Walls

This study aims to explore the effects grooved walls have on the discharge performance characteristics of a hall-effect thruster. The authors obtain measurements of electron conductivity as well as ionization distribution [14]. This data is then analyzed, with their findings being as follows:

- When groves are used in the section of the walls where ionization occurs, the electron transit time is shortened, leading to a decrease in thrust resulting from plume divergence.

- When groves are used in the acceleration region of the walls, electron transport current is significantly increased.
- Groves have an overall negative effect on discharge performance.

1.3 Project Proposal

The goal of this study is to optimize the performance of existing high-power Hall-Effect Thrusters (HETs). The optimization parameters include, but are not limited to, power draw, thrust, most optimal propellant type, and channel wall material. The optimization conducted in this study will be compared against existing technologies every step of the way to validate improvements to the various parameters. I addition to validation against current HETs, comparisons against chemical thrusters will be made to contrast the overall performance of both types of systems.

1.4 Methodology

Due to the prohibitive nature of building a physical hall-effect thruster for testing purposes as well as the severe lack of expertise to do so, simulation software – COMSOL Multiphysics and MATLAB in particular - will be used. The first step in the process will be to gather and review as much published data as possible on the current state of HETs in terms of their thrust output, power requirements and generators, types of fuels used as well as their advantages and disadvantages. Next, a model with the gathered data will be constructed to produce a baseline of performance characteristics of current state-of-the-art HETs, which will then be used to validate the performance of the theoretical model produced in this study.

For the theoretical model, a geometric 2D model will be produced in COMSOL for each component that is to be optimized to visually and numerically gather the required data. This data is then used in MATLAB to construct visual representations of the data produced from the various changes in parameters that will be introduced. In conjunction with the above, a non-dominating sorting genetic algorithm (NSGA-II) will be used to further assist in the optimization process objectives. An example of this will be the observance of changes in plots and graphs when the power supplied to the system changes from one value to another. With every step, the theoretical model will be validated against the benchmark to make sure the solution is realistic and/or makes sense.

Chapter 2 - Hall-Effect Thruster Background

2.1 Introduction

Consisting primarily of three main components: A channel containing an anode, a magnetic field generator, and an external cathode, hall-effect thrusters are well known for their relative simplicity. The physics that allows them to produce thrust, however, is much more complex than in other electric propulsion systems. This means that any small change in any of the thruster component parameters usually has a drastic effect on its performance. This includes, but is not limited to, the shape of the magnetic field, the materials of the channel wall as well as the type of propellant used.

A common characteristic of hall-effect thrusters is their inferior efficiency and specific impulse when compared to other types of ion thrusters. This drawback, however, is vastly outweighed by their higher thrust-to-weight ratio and lower number of operating power supplies. Additionally, their higher throughput makes hall-effect thrusters an ideal candidate for countless applications.

There are two types of hall-effect thrusters in existence. The first uses a dielectric insulating wall within the plasma channel that is typically made out of boron nitride or borosil. Those types of insulating materials are generally used for flight-ready thrusters, while other materials such as alumina are used in laboratory thrusters. Figure 2.1 shows a schematic of the cross-section of a dielectric thruster.

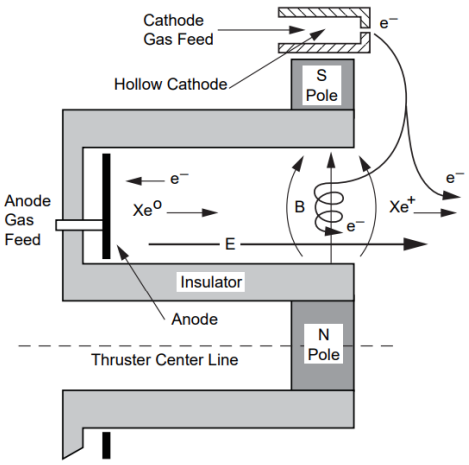

Figure 2.1 – Dielectric hall-effect thruster [1]

The second type of thruster, called thruster with anode layer (TAL), uses a metallic conducting wall instead. This material change alters the geometry of the thruster and shortens the ion acceleration channel, as shown in figure 2.2. This, however, does not change the ion generation or acceleration methods, but it does mean that the magnetic circuit demands negative bias to reduce electron power losses by repelling electrons in the ionization region [1].

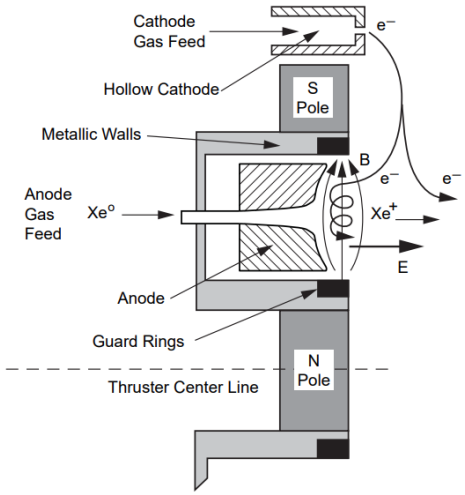

Figure 2.2 –TAL thruster [1]

Dielectric wall-based thrusters produce an axial electric field between the anode and the hollow-cathode plasma that is produced outside of the thruster channel. A radial magnetic field is also produced whose purpose is to prevent electrons from streaming directly into the anode [1]. The method by which electrons reach the anode is through the transverse magnetic field lines. This method prevents electron-electron and electron-channel wall collisions, which significantly improves ionization efficiency.

The plasma that is produced within the channel walls ionizes the propellant inflowing from the anode region with a high degree of efficiency. The ions produced then go on to bombard the walls themselves near the channel exit, which eventually erode the dielectric walls. This is a major determinant of the longevity of a thruster.

Similar to dielectric-wall thrusters, TAL thrusters produce an axial electric field between the annular channel and the plasma present outside of the thruster channel. Radial magnetic lines guide electrons to the anode to prevent collisions as was the case with dielectric-wall thrusters.

Where the two designs begin to diverge is in the choice of material of the walls and the rings at the channel exit. TAL design uses metal, which reduces electron loss along the magnetic field lines [1].

2.2 Performance

2.2.1 Efficiency

The efficiency calculation of hall-effect thrusters begins by relating the gas flow inside the anode and cathode and is represented by the following equation:

$$\dot{m}_p = \dot{m}_a + \dot{m}_c \tag{2.1}$$

Because in a hall-effect thruster, the cathode gas is injected outside of the discharge channel and is generally lost, the cathode efficiency is therefore represented by

$$\eta_c = \frac{\dot{m}_a}{\dot{m}_p} = \frac{\dot{m}_a}{\dot{m}_a + \dot{m}_c} \tag{2.2}$$

The power into the thruster is thus considered by the following formula:

$$P_{\text{in}} = P_d + P_k + P_{\text{mag}} \tag{2.3}$$

This then leads to the equation that describes the electrical utilization efficiency for power used to power the rest of the systems in a hall-effect thruster and is described by

$$\eta_o = \frac{P_d}{P_T} = \frac{P_d}{P_d + P_k + P_{\text{mag}}} \tag{2.4}$$

The full expression for the total efficiency then becomes

$$\eta_T = \frac{1}{2}\frac{T^2}{\dot{m}_a P_d}\eta_c \eta_o \tag{2.5}$$

2.2.2 Power Loss

In a hall-effect thruster, the power is supplied into the thruster from the discharge power supply. The power supplied out of the thruster is given by

$$P_d = P_b + P_w + P_a + P_R + P_{\text{ion}} \tag{2.6}$$

In dielectric-wall thrusters, the most significant power loss occurs due to electron and ion currents flowing along the radial magnetic field through the sheath to the channel walls [1]. This loss can be estimated from the sheath potential and the electric fields in the plasma.

2.2.3 Electron Temperature

Electron temperature is an important aspect when it comes to the performance of a thruster because it is a direct function of power loss; additionally, to calculate the power loss in a system, the electron temperature must be known. One of the major challenges in doing so is the fact that electron temperatures vary from region to region along the channel. With that in mind, it is known that the highest electron temperature occurs in the region with the strongest magnetic field. This region is generally near the channel exit.

2.2.4 Dielectric Walls Efficiency

Dielectric walls have a substantial effect on the efficiency of a thruster. This efficiency can be calculated using the total power-loss equation previously calculated, where the value for the effective electrical efficiency is obtained [1]. This is described mathematically by the following equation:

$$P_w = I_{iw}\left[\left(\frac{2M}{\pi m}\right)^{1/2} e^{e\phi_s/kT_e}\left(\frac{kT_e}{e}\right)+\left(\varepsilon-\phi_s\right)\right] \tag{2.7}$$

2.2.5 Thrust

In hall-effect thrusters, as in all types of propulsion, thrust is what moves a spacecraft. The thrust equation is given by the following:

$$T = \frac{d}{dt}\left(m_p v_{\text{ex}}\right) = \frac{dm_p}{dt}\, v_{\text{ex}} = \dot{m}_p v_{\text{ex}} \tag{2.8}$$

In this equation, $\dot{m}_{\text{p}}$ is the propellant mass flow rate. This is related to the kinetic thrust power, or jet power, by the following equation:

$$P_{\text{jet}} = \frac{1}{2}\dot{m}_p v_{\text{ex}}^2 \tag{2.9}$$

This equation can then be reduced to

$$P_{\text{jet}} = \frac{T^2}{2\dot{m}_p} \tag{2.10}$$

The aforementioned equation shows that an increase in jet power occurs if there is an increase in thrust without an increase in the propellant flow rate. In hall and ion thrusters, ions are accelerated to high velocities through a power source. This ion velocity vastly exceeds the velocities of any unionized ions that may escape the thruster [1], which is described by the following equation:

$$T = \frac{dm_p}{dt} v_{\text{ex}} \approx \dot{m}_i v_i \tag{2.11}$$

Where the ion exhaust velocity in terms of the net voltage of the ion acceleration, charge, and mass is given by

$$v_i = \sqrt{\frac{2qV_b}{M}} \tag{2.12}$$

The combined thrust equation for a singly charged propellant can then be expressed as

$$T = \sqrt{\frac{2M}{e}}\, I_b \sqrt{V_b} \tag{2.13}$$

The equation above describes the thrust of a unidirectional singly ionized, monoenergetic beam of ions [1]. For practical purposes, this equation must be modified to account for the divergence in the ion beam as well as the presence of charged ions within electric thrusters. Therefore, the aforementioned equation is only an approximation of the thrust output.

2.2.6 Specific Impulse

The ratio of thrust to the rate of consumption of propellant is termed as the specific impulse, or Isp [1]. When Xenon is used as the propellant of choice, such as the case in most hall-effect thrusters, the equation that describes the specific impulse is as follows:

$$\text{Isp} = \frac{T}{\dot{m}_p g} \tag{2.14}$$

Where g is the gravitational constant. When the effective exhaust velocity, v_{ex}, is introduced, the specific impulse equation then becomes

$$\text{Isp} = \frac{v_{ex}}{g} \tag{2.15}$$

When the singly charged thrust from the previous section is introduced, the specific impulse for the propellant unitization efficiency is then expressed by

$$\text{Isp} = \frac{\gamma \eta_m}{g} \sqrt{\frac{2eV_b}{M}} \tag{2.16}$$

Where V_b is the beam voltage in volts and M is the ionic mass in atom mass units.

Chapter 3 - Physics

3.1 Governing Equations

The behavior of plasma within hall-effect thrusters can be modeled by the Energy, Momentum, and Continuity equations, otherwise known as the governing equations of fluid dynamics. This set of three equations describes the three physical parameters upon which fluid dynamics is built and are summed as follows: Energy is conserved, Newton's Second Law holds, and mass is conserved. In this section, a derivation of each equation will be performed per J.D. Anderson's *Computational Fluid Dynamics: An Introduction* [15].

3.1.1 Energy

The energy equation describes the physical phenomenon which states that energy can neither be created nor destroyed. With this in mind, the derivation of the energy equation begins by using an infinitesimal fluid element, as shown in figure 3.1.

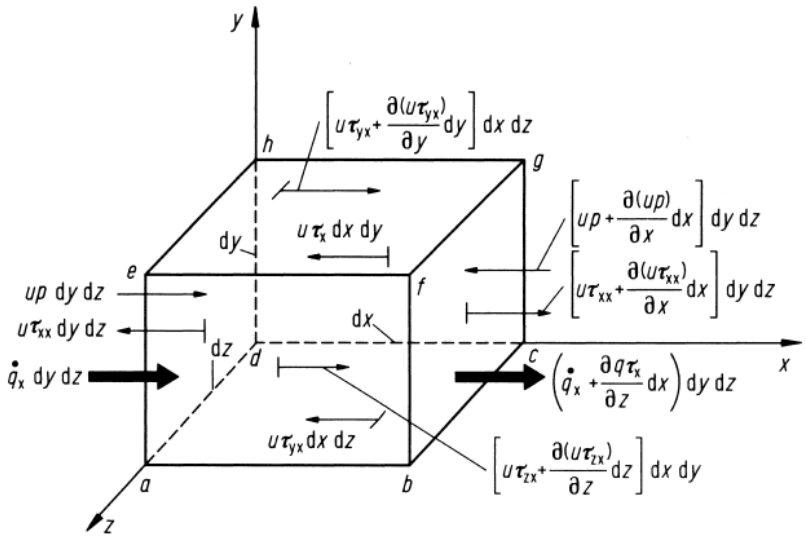

Figure 3.1 – Energy flux of an infinitesimally small fluid element [15]

This element is assumed to be moving, with its movement described by the following:

$$\left\{\begin{array}{l}\text{Rate of change of}\\ \text{energy inside the}\\ \text{fluid element}\end{array}\right\} = \left\{\begin{array}{l}\text{Net flux of}\\ \text{heat into}\\ \text{the element}\end{array}\right\} + \left\{\begin{array}{l}\text{Rate of working done on}\\ \text{the element due to body}\\ \text{and surface forces}\end{array}\right\}$$

First, an expression for the rate of work done on the element due to body and surface forces is obtained by assuming that the product of the force and the component of velocity in the direction of the force is equal to the rate of doing work by a force [15]. This can be mathematically expressed as

$$\rho \vec{f} \cdot \vec{V}(\mathrm{d}x\ \mathrm{d}y\ \mathrm{d}z) \tag{3.1}$$

If we consider the work done in the *x*-direction, it is evident that the work done is simply the *x*-component of the velocity multiplied by the pressure and shear forces. This holds for any other direction that is investigated. Now, if the net work done by the pressure in a particular direction is required, i.e. the *x*-direction, according to figure 3.1, it can be represented as

$$\left[up - \left(up + \frac{\partial(up)}{\partial x}\mathrm{d}x\right)\right]\mathrm{d}y\ \mathrm{d}z = -\frac{\partial(up)}{\partial x}\mathrm{d}x\ \mathrm{d}y\ \mathrm{d}z \tag{3.2}$$

Additionally, if the net work done by the shear force is required, it is represented as

$$\left[-\frac{\partial(up)}{\partial x} + \frac{\partial(u\tau_{xx})}{\partial x} + \frac{\partial(u\tau_{yx})}{\partial y} + \frac{\partial(u\tau_{zx})}{\partial z}\right]\mathrm{d}x\ \mathrm{d}y\ \mathrm{d}z \tag{3.3}$$

Finally, the net rate of work done on the moving element in all directions can be expressed as

$$\left[-\left(\frac{\partial(up)}{\partial x}+\frac{\partial(vp)}{\partial y}+\frac{\partial(wp)}{\partial z}\right)+\frac{\partial(u\tau_{xx})}{\partial x}+\frac{\partial(u\tau_{yx})}{\partial y}+\frac{\partial(u\tau_{zx})}{\partial z}+\frac{\partial(v\tau_{xy})}{\partial x}+\frac{\partial(v\tau_{yy})}{\partial y}+\frac{\partial(v\tau_{zy})}{\partial z}+\frac{\partial(w\tau_{xz})}{\partial x}+\frac{\partial(w\tau_{yz})}{\partial y}+\frac{\partial(w\tau_{zz})}{\partial z}\right]\mathrm{d}x\,\mathrm{d}y\,\mathrm{d}z+\rho\vec{f}\cdot\vec{V}\,\mathrm{d}x\,\mathrm{d}y\,\mathrm{d}z \tag{3.4}$$

Now special attention should be paid to the net heat flux on the element. This heat flux is due to two sources: radiation and thermal conduction [15]. Similar to the work equations above, the net heat on the element by thermal conduction in the *x*-direction is expressed by

$$\left[\dot{q}_x-\left(\dot{q}_x+\frac{\partial\dot{q}_x}{\partial x}\mathrm{d}x\right)\right]\mathrm{d}y\,\mathrm{d}z=-\frac{\partial\dot{q}_x}{\partial x}\mathrm{d}x\,\mathrm{d}y\,\mathrm{d}z \tag{3.5}$$

Similarly, the net heat on the element in all directions is expressed by

$$\left[\rho\dot{q}-\left(\frac{\partial\dot{q}_x}{\partial x}+\frac{\partial\dot{q}_y}{\partial y}+\frac{\partial\dot{q}_z}{\partial z}\right)\right]\mathrm{d}x\,\mathrm{d}y\,\mathrm{d}z \tag{3.6}$$

Where the local temperature gradient is

$$\dot{q}_x=-k\frac{\partial T}{\partial x};\qquad \dot{q}_y=-k\frac{\partial T}{\partial y};\qquad \dot{q}_z=-k\frac{\partial T}{\partial z}$$

Finally, combining and plugging the above equations into

$$\rho\frac{D}{Dt}\left(e+\frac{V^2}{2}\right)\mathrm{d}x\,\mathrm{d}y\,\mathrm{d}z \tag{3.7}$$

results in the final form of the energy equation, represented by

$$\rho\frac{D}{Dt}\left(e+\frac{V^2}{2}\right)=\rho\dot{q}+\frac{\partial}{\partial x}\left(k\frac{\partial T}{\partial x}\right)+\frac{\partial}{\partial y}\left(k\frac{\partial T}{\partial y}\right)+\frac{\partial}{\partial z}\left(k\frac{\partial T}{\partial z}\right) \tag{3.8}$$
$$-\frac{\partial(up)}{\partial x}-\frac{\partial(vp)}{\partial y}-\frac{\partial(wp)}{\partial z}+\frac{\partial(u\tau_{xx})}{\partial x}+\frac{\partial(u\tau_{yx})}{\partial y}$$
$$+\frac{\partial(u\tau_{zx})}{\partial z}+\frac{\partial(v\tau_{xy})}{\partial x}+\frac{\partial(v\tau_{yy})}{\partial y}+\frac{\partial(v\tau_{zy})}{\partial z}$$
$$+\frac{\partial(w\tau_{xz})}{\partial x}+\frac{\partial(w\tau_{yz})}{\partial y}+\frac{\partial(w\tau_{zz})}{\partial z}+\rho\vec{f}\cdot\vec{V}$$

3.1.2 Continuity

The continuity equation involves both a finite control volume and infinitesimal fluid element models [15]. In this section, both models are explored, where the finite control volume is to be fixed, and the infinitesimal fluid element is to be moving. A comparison between the two can then be easily made. Starting with the moving fluid element model, the mass and volume can be represented by

$$\delta m=\rho\delta\mathcal{V} \tag{3.9}$$

Because of the conservation of mass, the mass of the element does not change as it flows with the fluid. This is expressed by the derivative

$$\frac{D(\delta m)}{Dt}=0 \tag{3.10}$$

When the above two equations are combined, the result is the non-conservative continuity equation, represented as:

$$\frac{D\rho}{Dt}+\rho\nabla.\vec{V}=0 \tag{3.11}$$

Next, the fixed-in-space control volume model is explored, as sketched in figure 3.2.

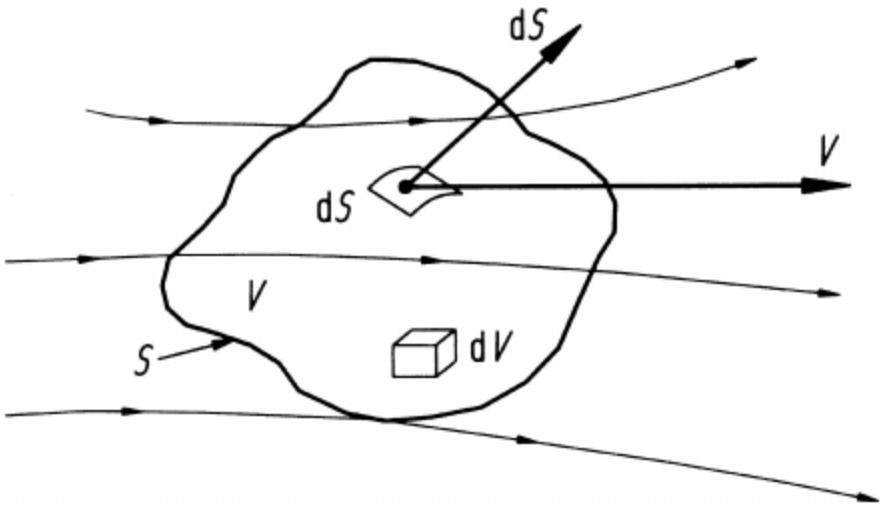

Figure 3.2 – Finite control volume [15]

The mass flow of a fluid element moving across a fixed surface is the density multiplied by the area of the surface multiplied by the velocity perpendicular to the surface [15]. This is mathematically represented as

$$\rho V_{\mathrm{n}} \mathrm{d}S = \rho \vec{V} \cdot \vec{\mathrm{d}}S \tag{3.12}$$

When special attention is paid to the control volume in figure 3.2, it becomes clear that a negative $\rho \vec{V} \cdot \vec{\mathrm{d}}S$ means an inflow into the control volume, while a positive means an outflow.

This means that the net mass flow into the volume is the sum over S of the elemental mass flow, which can be expressed by

$$\oiint_S \rho \vec{V} \cdot \vec{\mathrm{d}}S \tag{3.13}$$

If there is an increase in change over time of the total mass inside the control volume, the equation is then

$$-\frac{\partial}{\partial t} \iiint_{\mathcal{V}} \rho \, \mathrm{d}\mathcal{V} \tag{3.14}$$

Finally, when the above equations are plugged in, the integral-conservation form of the continuity equation is derived as the following:

$$\frac{\partial}{\partial t}\iiint_{\mathscr{V}} \rho \, \mathrm{d}\mathscr{V} + \oiint_{S} \rho \vec{V} \cdot \vec{\mathrm{d}}S = 0 \tag{3.15}$$

3.1.3 Momentum

The momentum equation employs the physical principle described by Newton's Second Law, which shows that the net force on a fluid element equals the mass times the acceleration of that element [15]. It should be kept in mind that this is a vector relation, which could be split into three scalar values in the *x*, *y*, and *z* directions as needed. First, let us assume that the *x*-component is required. Newton's Second Law then becomes

$$F_x = ma_x \tag{3.16}$$

If the left side of the equation is considered to be all the surface and body forces acting on the element in the *x*-direction, it is evident that in the case of body forces, the shear stresses involve the deformation of the fluid element in terms of time rate-of-change. As for the normal stresses, the time rate-of-change occurs in terms of the volume of the element [15]. Figure 3.3 below shows both cases.

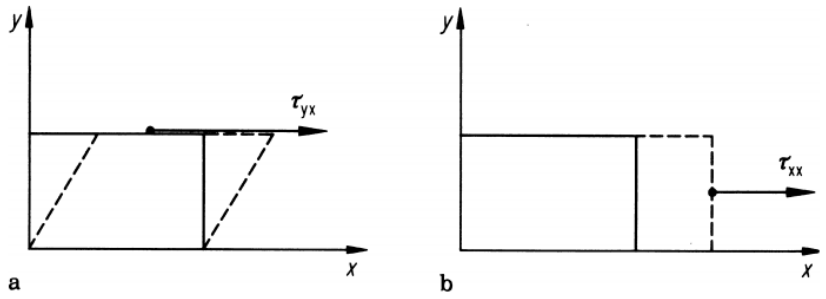

Figure 3.3 – Shear (a) and normal (b) stresses [15]

Now the aforementioned can finally be translated into the following mathematical expression:

$$\left\{\begin{matrix}\text{Net surface force}\\ \text{in the } x\text{-direction}\end{matrix}\right\} = \left[p - \left(p + \frac{\partial p}{\partial x}\mathrm{d}x\right)\right]\mathrm{d}y\ \mathrm{d}z + \left[\left(\tau_{xx} + \frac{\partial \tau_{xx}}{\partial x}\mathrm{d}x\right) - \tau_{xx}\right]\mathrm{d}y\ \mathrm{d}z + \left[\left(\tau_{yx} + \frac{\partial \tau_{yx}}{\partial y}\mathrm{d}y\right) - \tau_{yx}\right]\mathrm{d}x\ \mathrm{d}z + \left[\left(\tau_{zx} + \frac{\partial \tau_{zx}}{\partial z}\mathrm{d}z\right) - \tau_{zx}\right]\mathrm{d}x\ \mathrm{d}y$$

This then leads to the total force in the *x*-direction, expressed as:

$$F_x = \left(-\frac{\partial p}{\partial x} + \frac{\partial \tau_{xx}}{\partial x} + \frac{\partial \tau_{yx}}{\partial y} + \frac{\partial \tau_{zx}}{\partial z}\right)\mathrm{d}x\ \mathrm{d}y\ \mathrm{d}z + \rho f_x\ \mathrm{d}x\ \mathrm{d}y\ \mathrm{d}z \tag{3.17}$$

Now that the left-hand side of the force equation has been taken care of, special attention is now paid to the right-hand side, where the mass of the fluid element, *m*, is fixed and represented by:

$$m = \rho\ \mathrm{d}x\ \mathrm{d}y\ \mathrm{d}z \tag{3.18}$$

Furthermore, the acceleration in the *x*-direction is the time rate-of-change of the velocity and is expressed by:

$$a_x = \frac{Du}{Dt} \tag{3.19}$$

When combined, the *x*-component of the momentum equation is achieved as:

$$\rho\frac{Du}{Dt} = -\frac{\partial p}{\partial x} + \frac{\partial \tau_{xx}}{\partial x} + \frac{\partial \tau_{yx}}{\partial y} + \frac{\partial \tau_{zx}}{\partial z} + \rho f_x \tag{3.20}$$

Following the previous steps, the *y* and *z* components of the momentum equation can also be achieved as:

x-direction:
$$\rho\frac{Dv}{Dt} = -\frac{\partial p}{\partial y} + \frac{\partial \tau_{xy}}{\partial x} + \frac{\partial \tau_{yy}}{\partial y} + \frac{\partial \tau_{zy}}{\partial z} + \rho f_y \tag{3.21}$$

y-direction:
$$\rho\frac{Dw}{Dt} = -\frac{\partial p}{\partial z} + \frac{\partial \tau_{xz}}{\partial x} + \frac{\partial \tau_{yz}}{\partial y} + \frac{\partial \tau_{zz}}{\partial z} + \rho f_z \tag{3.22}$$

This derived list of equations describes the three components of the momentum equation in partial differential, non-conservation form. These are what are commonly known as the Navier-Stokes equations. To achieve the conservation form of this set of equations, several steps are performed. First, using the equation

$$\rho\frac{Du}{Dt} = \rho\frac{\partial u}{\partial t} + \rho\vec{V}\cdot\nabla u \tag{3.23}$$

and expanding the following derivative

$$\frac{\partial(\rho u)}{\partial t} = \rho\frac{\partial u}{\partial t} + u\frac{\partial \rho}{\partial t} \tag{3.24}$$

yields a vector divergence identity, represented by

$$\nabla\cdot(\rho u\vec{V}) = u\nabla\cdot(\rho\vec{V}) + (\rho\vec{V})\cdot\nabla u \tag{3.25}$$

After substitution, the following two equations are achieved:

$$\rho\frac{Du}{Dt} = \frac{\partial(\rho u)}{\partial t} - u\frac{\partial \rho}{\partial t} - u\nabla\cdot(\rho\vec{V}) + \nabla\cdot(\rho u\vec{V})$$
$$\rho\frac{Du}{Dt} = \frac{\partial(\rho u)}{\partial t} - u\left[\frac{\partial \rho}{\partial t} + \nabla\cdot(\rho\vec{V})\right] + \nabla\cdot(\rho u\vec{V})$$

Where the equation inside the brackets is the left-hand side of the continuity equation [15], which makes it zero. This leads to the following reduced expression:

$$\rho\frac{Du}{Dt} = \frac{\partial(\rho u)}{\partial t} + \nabla\cdot(\rho u\vec{V}) \tag{3.26}$$

Finally, after the substitution, the list of Navier-Stokes equations in conservation form is expressed as follows:

x-direction: $$\frac{\partial(\rho u)}{\partial t} + \nabla\cdot(\rho u\vec{V}) = -\frac{\partial p}{\partial x} + \frac{\partial \tau_{xx}}{\partial x} + \frac{\partial \tau_{yx}}{\partial y} + \frac{\partial \tau_{zx}}{\partial z} + \rho f_x \tag{3.27}$$

y-direction: $$\frac{\partial(\rho v)}{\partial t} + \nabla\cdot(\rho v\vec{V}) = -\frac{\partial p}{\partial y} + \frac{\partial \tau_{xy}}{\partial x} + \frac{\partial \tau_{yy}}{\partial y} + \frac{\partial \tau_{zy}}{\partial z} + \rho f_y \tag{3.28}$$

z-direction: $$\frac{\partial(\rho w)}{\partial t} + \nabla\cdot(\rho w\vec{V}) = -\frac{\partial p}{\partial z} + \frac{\partial \tau_{xz}}{\partial x} + \frac{\partial \tau_{yz}}{\partial y} + \frac{\partial \tau_{zz}}{\partial z} + \rho f_z \tag{3.29}$$

Chapter 4 – Parametric Studies

4.1 Introduction

Though technologically mature and form the backbone of numerous applications, hall-effect thrusters (HET) come with some uniquely misunderstood physical phenomena. One such phenomenon is the interaction of the particles within the discharge plasma [16]. This shortcoming in full understanding of this unique physical phenomenon contributes to the widespread lack in the development of accurate and reliable rare-field plasma discharge interaction models.

This portion of the paper presents two unique parametric studies. The first deals specifically with the interaction of primary and secondary electrons between the walls and radial and axial magnetic fields, while the second study deals with a general overview of the improvement of various parameters.

4.2 Radial Plasma Wall Study

4.2.1 Theory

This study investigates the 1D radial plasma wall model as introduced by Dominguez-Vasquez, Taccogna, and Ahedo [17]. The model analyzes the plasma structure at different regions within the acceleration chamber while considering the weak plasma collisions between the walls and the electrons. Figure 4.1 shows an overview of this model.

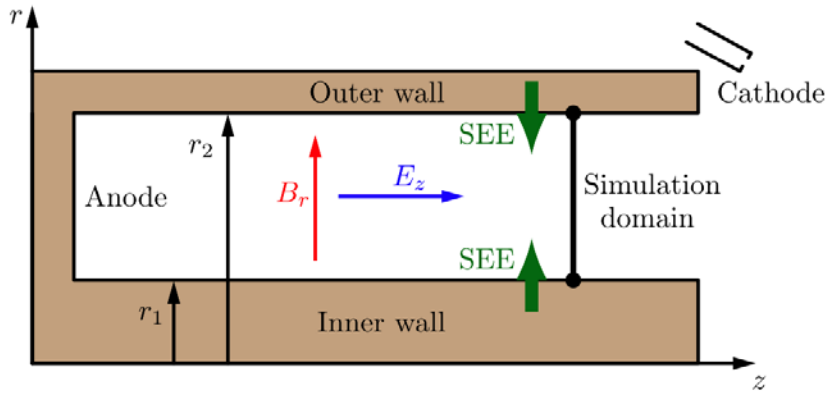

Figure 4.1 – 1D model [17]

The particles in this model are modeled as macroparticle populations, with electrons and singly-charged ions being the main particle types. Additionally, neutrals are also present and are modeled as spatially uniform with constant temperature, but time-dependent density. The weight of every particle within each population is considered the same and does not change throughout the simulation. Here the desired discharge simulation is quasi-stationary with an average density. This is represented by the following reduced 1D ion and electron conservation equation [17].

$$\frac{\partial n_j}{\partial t} + \frac{1}{r}\frac{\partial}{\partial r}(r n_j u_{rj}) = S_{\text{ioniz}} + S_{\text{axial},j}, \quad j = \text{i, e,} \tag{4.1}$$

In the preceding equation, n_j and u_{rj} represent the radial flux. S_{ioniz} represents the ionization source term, while $S_{axial,j}$ represents the net axial contribution term. To achieve a quasi-stationary discharge, the losses of the channel wall must be balanced by the ionization and axial source terms [16]. This means that the net axial contribution term becomes zero, which negates the need for external axial plasma contribution.

The 1D model in this study assumes the presence of an axial electric field, E_z, which accelerates the ions with respect to time. This is an undesirable effect in the simulation. Other simulations have dealt with this issue by frequently resetting the particle population. In this simulation, however, this effect will be ignored for the time being. Thus, E_z will be assumed to only affect ions in the radial direction. The force of this electric field is then expressed by the following:

$$E_r = \frac{-d\phi}{dr} \tag{4.2}$$

Where $\phi(r,t)$ is the electric potential.

The next point of interest is the interaction between the plasma and the channel wall. The plasma particles (ions and electrons) are collected as they reach the walls [17]. Here, the secondary electron emission produced by the collisions follows a probability model that is divided into three

different types: elastic, non-elastic, and exact. In this study only the exact model is considered and is represented by the following formula:

$$\delta_{TS}\,(E) \approx \frac{E}{E_c} \tag{4.3}$$

Where E represents the electron collision energy and E_c represents the crossover energy.

The collision interactions of the particles as presented in [17] are modeled as electron-neutral, electron-ion, and ion-ion Coulomb collisions, with ion-neutral collisions being negligible. Additionally, the secondary electrons that are produced during the collisions are assumed to transfer to the primary electron population when they collide with neutral particles within the plasma.

4.2.2 Numerical Simulation

The numerical simulation for this study uses a particle-in-cell regime and is heavily based on the study published by Vazquez, Taccogna, and Ahedo [17]. Xenon is used as the propellant, with parameters such as fluxes and particle densities being computed at the nodes of the mesh using an average-weighted method. The mesh itself is uniform with cell size smaller than the plasma Debye length [17]. As aforementioned, the macroparticles within the plasma are assumed to have the same weight throughout the simulation, with the number of particles being 70 per cell. The following table presents the main input parameters, applied forces, grid, and population settings in the initial model as introduced in [17].

Table 1 – Parameter values

Type	Description	Symbol	Units	Value
Population settings	Number of elementary particles per macroparticle	W	—	$3 \cdot 10^9$
	Initial r-averaged plasma density	$\bar{n}_{e0}$	10^{17} m^{-3}	0.8
	Initial number of ion/electron macroparticles*	N_{p0}	—	106814
	Initial electron temperature	T_{e0}	eV	10
	Initial ion temperature	T_{i0}	eV	1
	Ion axial mean velocity	u_{zi}	km s^{-1}	10
	Initial background neutral density	n_{n0}	10^{17} m^{-3}	40
	Neutral temperature	T_n	K	700
***E*, *B* fields**	Electric field axial component	E_z	V cm^{-1}	100
	Magnetic field radial component at inner radius	B_{r1}	G	150
Simulation parameters	Inner radius	r_1	cm	3.5
	Outer radius	r_2	cm	5.0
	Number of nodes	N_r	—	1500
	Grid spacing*	Δr	μm	10
	Timestep	Δt	ps	5
Physical parameters	Debye length*	λ_D	μm	83.1
	Electron Larmor radius*	r_l	μm	802.0
	Inverse of plasma frequency*	$1/\omega_{pe}$	ps	62.7
	Inverse of electron cyclotron frequency*	$1/\omega_{ce}$	ps	379.1

Electric potential is obtained at the nodes through second-order finite-difference discretization schemes along the radial coordinates, with the Thomas algorithm being applied as the direct solver [17]. Electrons then begin to move in the corresponding direction of the axial and radial electric fields with respect to time, but only those moving in the radial direction are considered when updating the velocities and positions.

As the macroparticles advance in time by increments of timesteps, neutral-electron particle elastic and inelastic collisions start to occur. Such collisions produce new ions, to which mean axial velocity is added.

While the preceding table (table 1) shows the base values for the various parameters used in the simulation, which shall collectively be referred to as Case 1, table 2 [17] below shows the

list of variables in four other cases. The simulation results between the different cases are discussed in detail in the following sections.

Table 2 – Values of all five cases

Type	Description, symbol and units	Case 1	Changes from case 1
Populations settings	Number of elementary particles per macroparticle, W (-)	$3 \cdot 10^9$	Case 5: $7.06 \cdot 10^{13}$
	Initial average plasma density, n_{e0} (10^{17}m^{-3})	0.8	—
	Initial number of ions and electrons∗, N_{p0} (-)	106814	—
	Initial electron temperature, T_{e0} (eV)	10	—
	Initial ion temperature, T_{i0} (eV)	1	—
	Ion axial mean velocity, u_{zi} (km s^{-1})	10	—
	Initial background neutral density, n_{n0} (10^{17} m^{-3})	40	—
	Neutral temperature, T_n (K)	700	—
E, B fields	Electric field axial component, E_z (V/cm)	100	Case 2: 200
	Magnetic field radial component at inner radius, B_{r_1} (G)	150	Case 2: 300; Case 5: 124.84
Simulation parameters	Non-true-secondary emission	OFF	Case 3: ON
	True-secondary emission	ON	—
	Average true-secondary electrons emission energy, T_{eW} (eV)	2	Case 4: 0.2
	Inner radius, r_1 (cm)	3.5	Case 5: $10^5 + 3.5$
	Outer radius, r_2 (cm)	5.0	Case 5: $10^5 + 5.0$
	Number of nodes, N_r (-)	1500	—
	Grid spacing∗, Δr (μm)	10	—
	Timestep, Δt, (ps)	5	—
Physical parameters	Debye length∗, λ_D (μm)	83.1	—
	Electron Larmor radius∗, r_l (μm)	802.0	Case 2: 401.0; Case 5: 963.7
	Inverse of plasma frequency∗, $1/\omega_{pe}$ (ps)	62.7	—
	Inverse of electron cyclotron frequency∗, $1/\omega_{ce}$, (ps)	379.1	Case 2: 189.5; Case 5: 455.5

4.2.3 Results

The discussion in this section shall include the results of all five cases based on the differences of their respective input parameters. Case 1 will be considered the reference case, while cases 2 to 5 will be validated against it. In case 2 the parameters for the electric and magnetic fields are both doubled. In case 3, secondary, backscattered electrons are observed. In case 4, colder emission of exact electrons is investigated. Finally, in case 5, an analysis of planar discharge is conducted.

The primary function of case 2 is to validate the reliability of the code's ability to reproduce the electron dynamics [16]. Consequently, when doubling the magnetic and electric fields from case 1, it is correctly observed that the primary electron drift velocity remains the same, as shown in figure 4.2.3.1, while the secondary electron velocity also remains the same, as shown in figure 4.2. Furthermore, the secondary electrons produced by the walls perform double the number of

inner-wall orbits. The presence of double the number of peaks, when contrasted to case 1, proves this.

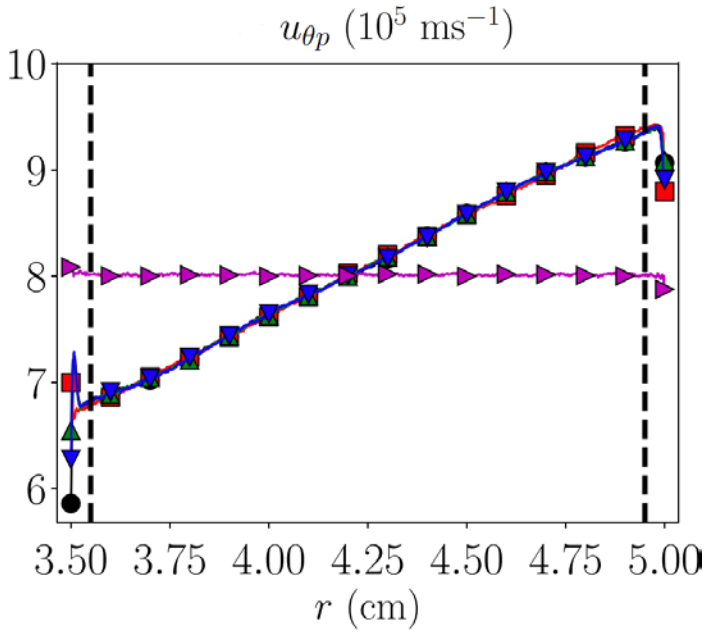

Figure 4.2 – Drift velocity [16]

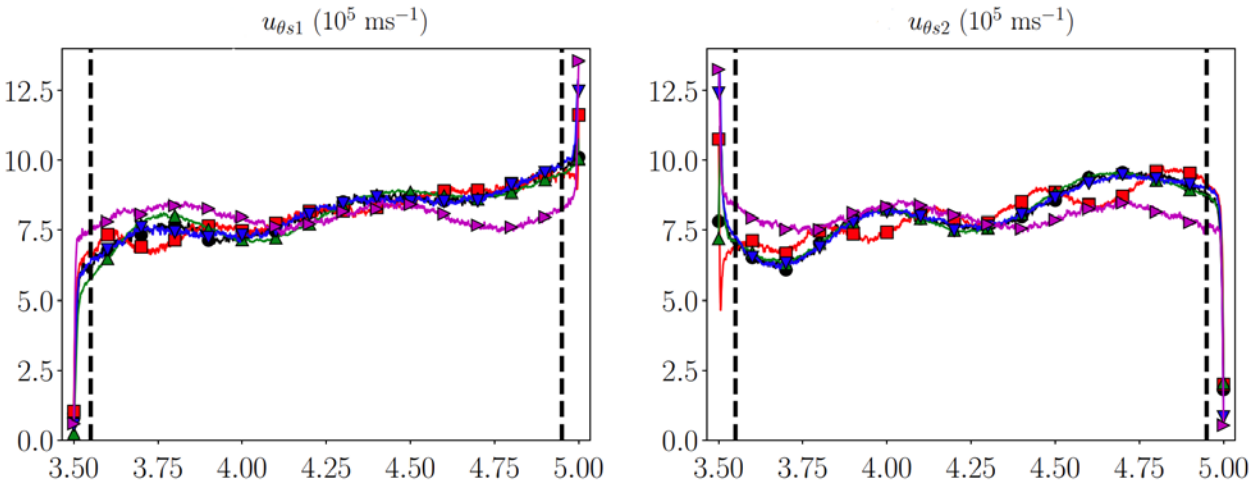

Figure 4.3 – Secondary electron drift velocity [16]

Compared to case 1, case 3 produces a much larger secondary electron emission. This acts to decrease the sheath potential by 0.5V in the inner walls and by 1.5V in the outer walls versus

case 1 [16]. This leads to a second electron density that is higher than that of case 1 by almost one order of magnitude. This is shown in figures 4.4, 4.5, and 4.6 below.

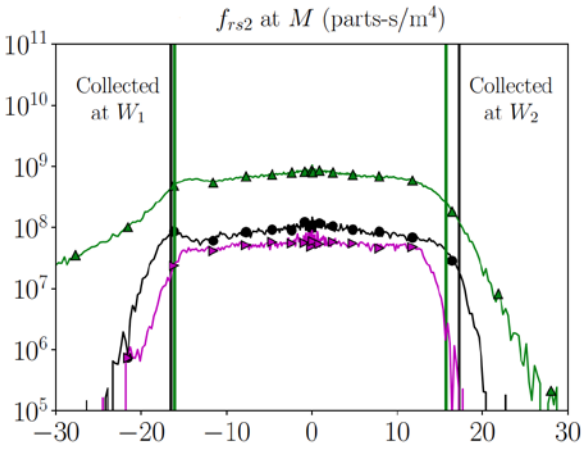

Figure 4.4 – Secondary electron emission [16]

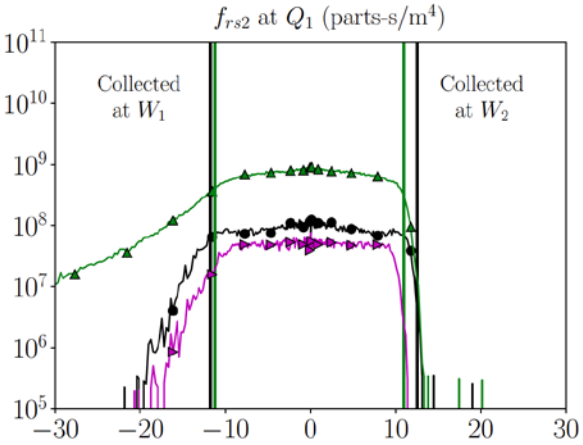

Figure 4.5 – Secondary electron emission [16]

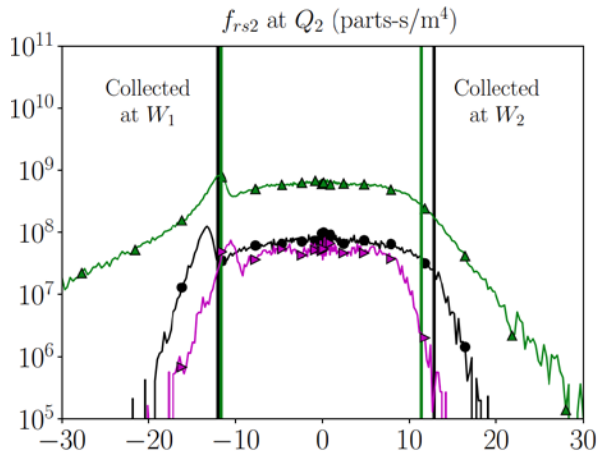

Figure 4.6 – Secondary electron emission [16]

In case 4, the energy produced by the secondary electron emission is about ten times lower than that of case 1. While this leads to lower temperature profiles, as shown in figures 4.7 and 4.8, it does not seem to affect the potential difference between the two walls. Because of their low wall-emission energy, electrons in case 4 tend to spend most of their time bouncing between the sheaths in a radial regime before collisions transfer them to the primary population [16].

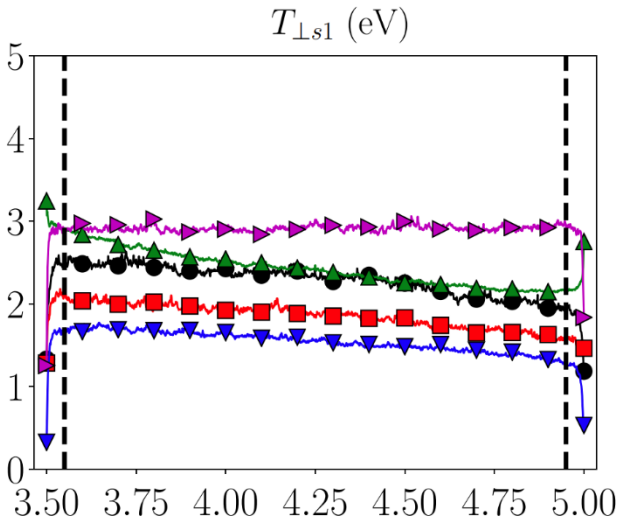

Figure 4.7 – Secondary electron temperature profile [16]

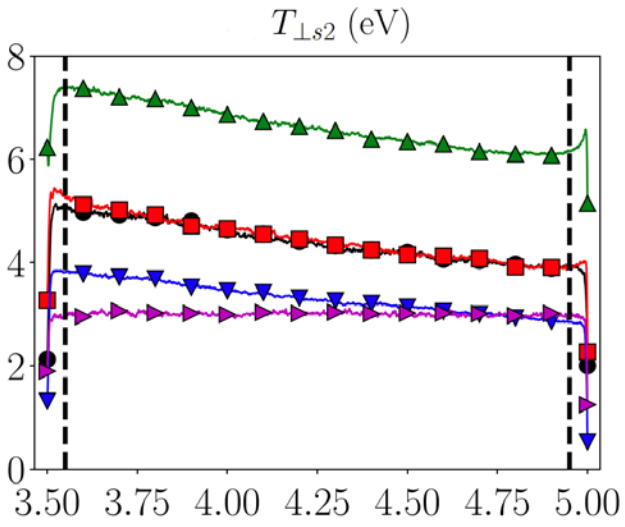

Figure 4.8 – Secondary electron temperature profile [16]

Case 5 involves planar discharge, in which a planar magnetic field is constant throughout, as shown in figures 4.9 and 4.10. Here the magnetic mirror is assumed negligible; therefore, the radial profile asymmetry at the walls consequently disappears for all-electron populations [16]. The temperature profile for this case also appears to follow the same regime as the previous four cases. Table 3 provides a compact overview of the results in all cases discussed.

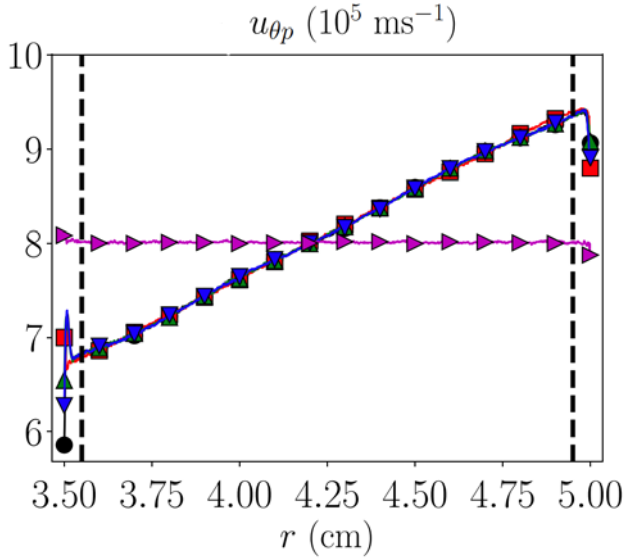

Figure 4.9 – S1 constant radial domain [16]

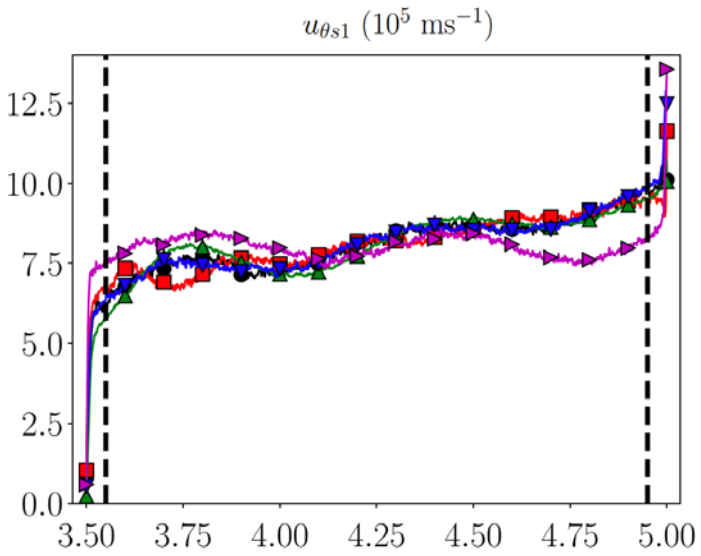

Figure 4.10 – S2 constant radial domain [16]

Table 3 – Cases 1-5 results

Electric potentials (V)	At the mid radius M, ϕ_M	17.69	17.24	16.09	17.34	14.48
	At the inner sheath edge Q_1, ϕ_{Q_1}	13.90	13.45	12.21	13.59	10.22
	At the outer sheath edge Q_2, ϕ_{Q_2}	12.86	12.50	11.36	12.64	10.14
	At the inner wall W_1, ϕ_{W_1}	2.22	2.21	1.03	2.31	−0.05
	At the outer wall W_2, ϕ_{W_2}	0.00	0.00	0.00	0.00	0.00
	p to the inner wall, $\lvert j_{p,1-}\rvert$	12.21	12.35	17.32	13.32	18.45
	$s1$ to the inner wall, $\lvert j_{s1,1-}\rvert$	0.18	0.23	1.66	0.23	0.22
Current densities (A m^{-2})	$s1$ from the inner wall, $\lvert j_{s1,1+}\rvert$	2.50	2.66	56.55	2.41	4.30
	$s2$ to the inner wall, $\lvert j_{s2,1-}\rvert$	3.57	3.52	51.31	2.38	1.80
	p to the outer wall, $\lvert j_{p,2+}\rvert$	23.16	23.61	55.46	24.24	18.13
	$s1$ to the outer wall, $\lvert j_{s1,2+}\rvert$	0.62	0.62	29.49	0.24	1.84
	$s2$ to the outer wall, $\lvert j_{s2,2+}\rvert$	0.88	0.75	21.27	0.58	0.24
	$s2$ from the outer wall, $\lvert j_{s2,2-}\rvert$	6.90	7.15	88.47	7.18	4.25
	e at the inner wall, $E_{we,1}$	7.92	8.90	12.51	8.18	11.34
	p at the inner wall, $E_{wp,1}$	8.51	9.07	8.51	8.43	11.74
Mean impact energies per elementary particle (eV)	$s1$ at the inner wall, $E_{ws1,1}$	5.09	3.74	4.13	3.53	3.81
	$s2$ at the inner wall, $E_{ws2,1}$	6.04	8.61	14.13	7.28	8.10
	e at the outer wall, $E_{e,2}$	15.50	15.61	13.89	15.55	11.43
	p at the outer wall, $E_{wp,2}$	16.00	15.99	13.76	15.90	11.86
	$s1$ at the outer wall, $E_{ws1,2}$	5.61	8.06	12.75	5.75	8.14
	$s2$ at the outer wall, $E_{ws2,2}$	9.39	10.15	15.84	4.91	4.07
	Non-true-secondaries at the inner wall, $\delta_{NTS,1}$	0.00	0.00	0.58	0.00	0.00
SEE yields (−)	True-secondary at the inner wall, $\delta_{TS,1}$	0.16	0.17	0.23	0.15	0.21
	Non-true-secondaries at the outer wall, $\delta_{NTS,2}$	0.00	0.00	0.58	0.00	0.00
	True-secondary at the outer wall, $\delta_{TS,2}$	0.28	0.29	0.25	0.29	0.21
Conversion to p and wall collection fractions (%)	$s1$ conversion to p	57.7	58.4	22.5	76.5	52.0
	$s1$ collection at the inner wall	7.1	8.5	3.0	9.5	5.2
	$s1$ collection at the outer wall	35.2	33.1	74.5	14.0	42.8
	$s2$ conversion to p	51.1	55.1	35.4	68.7	52.1
	$s2$ collection at the inner wall	36.2	34.4	40.6	23.2	42.4
	$s2$ collection at the outer wall	12.7	10.5	24.0	8.1	5.5
Replenishment parameter (−)	At the inner wall, $\sigma_{t,1}$	0.04	0.04	0.06	0.04	0.03
	At the outer wall, $\sigma_{t,2}$	0.05	0.04	0.10	0.05	0.03
Electron temperatures at M (eV)	p radial, $T_{rp,M}$	4.86	4.80	4.64	4.81	4.94
	p perpendicular, $T_{\perp p,M}$	7.52	7.58	7.39	7.47	7.78
	$s1$ radial, $T_{rs1,M}$	9.50	8.63	10.81	8.17	9.11
	$s1$ perpendicular, $T_{\perp s1,M}$	2.37	1.85	2.47	1.56	3.02
	$s2$ radial, $T_{rs2,M}$	9.77	9.87	10.37	9.07	9.04
	$s2$ perpendicular, $T_{\perp s2,M}$	4.45	4.59	6.61	3.26	3.02

4.2.4 Analysis

In this study, five cases involving the interaction of radial and dielectric walls were analyzed. Case 2, where the axial and radial magnetic fields were double that of case 1, illustrated two characteristics: First, it showed that secondary electrons are magnetized as soon as they are

emitted. Second, it demonstrated that numerical solution is achievable without change in macroscopic electron behavior.

Case 3 investigates the behavior of the secondary backscattered electrons and compares their behavior to those present in case 1. It is discovered that compared to case 1, the number of secondary electrons in case 3 is significantly greater in terms of emission volume and radial structure. Case 4 focuses on the exact secondary average electron emission [16], specifically the inner and outer wall difference in potential. It is implied that a magnetic mirror effect is present, which leads to a negligible potential asymmetry. As opposed to the other cases, case 5 investigates the planar plasma discharge. In this case, all asymmetries seem to disappear.

4.3 General Hall-Effect Thruster Study

4.3.1 Theory

The goal behind the general hall-effect thruster study is to achieve optimal discharge channel dimensions as well as an ideal specific impulse (I_{sp}) and thrust (T) by varying the voltage and discharge power. Thus, the general parameters used can be broken down into three main items: Channel width (w), diameter (d), and length (l). At this point in the study, a few assumptions have to be made: First, the thruster system in its entirety is considered a perfect or isolated system. This means that the system does not lose energy to its surroundings. Second, the system is adiabatic and isentropic. This assumes that system efficiency losses, propellant losses, thrust and power losses can be ignored. Third, xenon, the propellant gas, is considered constant and isothermal at every point in the channel. Finally, full conversion from potential to kinetic energy occurs. With this in mind, the following figures show a visual breakdown of the various parts of the thruster involved in this study.

Figure 4.11 shows the general schematic dimensions of the channel wall length, width, and diameter as well as the discharge channel dimensions, along with the position of the anode, cathode, and inner and outer magnetic coils.

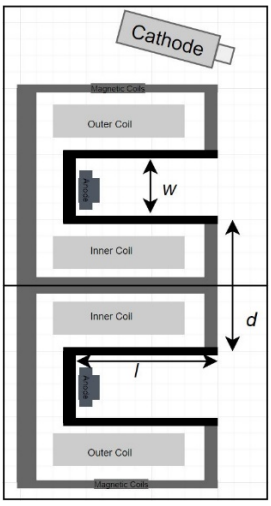

Figure 4.11 – Thruster schematic

Figure 4.12 shows the transit of the propellant from the point of its release within the cathode up to its interaction with the magnetic field and the anode gas inside the discharge channel.

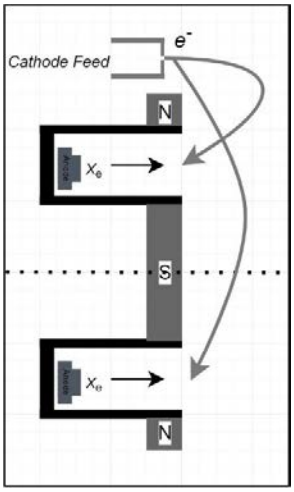

Figure 4.12 – Propellant release

Figure 4.13 demonstrates the interaction between the magnetic field and the electrons. Once the electrons encounter the radial and transverse magnetic fields, they begin to spiral in an E x B direction.

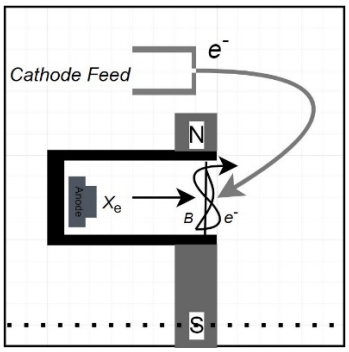

Figure 4.13 – Electron-magnetic field interaction

4.3.2 Performance Parameters

The performance parameters study for this system begins with choosing an arbitrary, but reasonable discharge voltage and input power. Anode mass flow rate, thrust, specific impulse, optimal channel diameter, length, and width are then obtained through the following formulations:

$$\text{Channel Diameter: } d = \sqrt{\frac{P}{633 * Ud}} \tag{4.4}$$

Where *P* is the input power and *Ud* is the discharge voltage.

$$\text{Channel Width: } w = 0.242 * d \tag{4.5}$$

$$\text{Anode Flow Rate: } \dot{m}_a = 0.003 * w * d \tag{4.6}$$

$$\text{Thrust: } T = 892.7 * 45.8 * \sqrt{Ud} \tag{4.7}$$

$$wd = \sqrt{\frac{P}{cpl}} \tag{4.8}$$

Where *P* is the input power and *cpl* is the pressure proportionality coefficient ($cpl = 1.2 * 10^6$).

$$\text{Channel Length: } l = \frac{Ct2 * \sqrt{Ud} * wd}{T} \tag{4.9}$$

$$\text{Specific Impulse: } I_{sp} = \frac{T}{\dot{m} * g} \tag{4.10}$$

Using the preceding list of equations, it is now possible to plot the different parameters to create a cohesive picture of the optimal values.

4.3.3 Results

The resulting sets of plots show the following relationships: Channel diameter, length, width versus power; channel length, diameter, width versus discharge voltage; anode flow rate versus power; anode flow rate versus discharge voltage; thrust versus power and final, thrust versus discharge voltage; specific impulse versus power and finally, specific impulse versus discharge voltage.

Starting with figures 4.14 and 4.15, it is observed that thruster diameter is a major contributor to the overall size of the system. Furthermore, there is a direct relationship between the diameter of the thruster and the power that it can withstand. This means that the larger the diameter, the more it can be incorporated. Additionally, an inverse relationship between the diameter of the thruster and the magnitude of the discharge voltage can also be observed. This relationship shows that as the diameter decreases, the discharge voltage increases and vice versa.

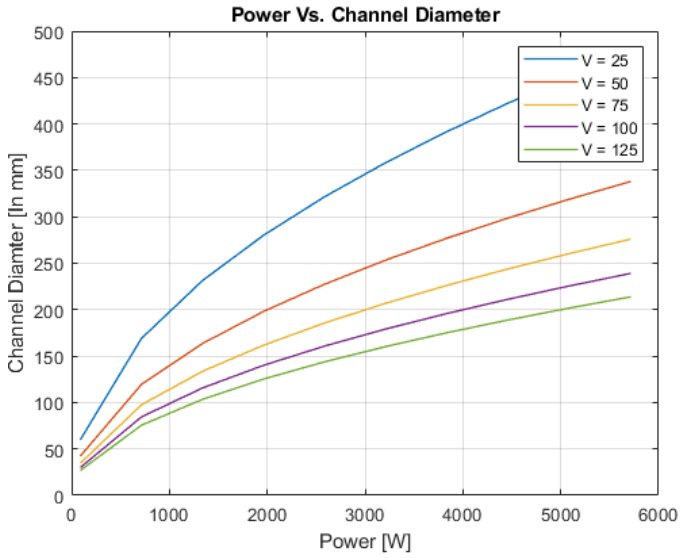

Figure 4.14 – Power-channel diameter relationship

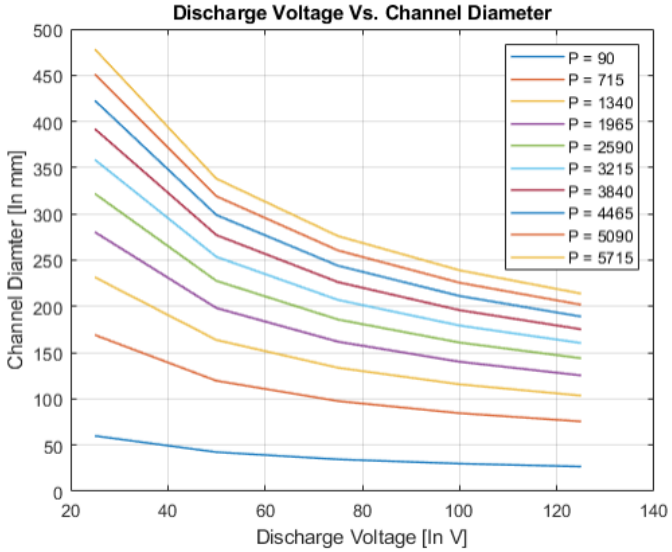

Figure 4.15 – Discharge voltage-channel diameter relationship

The second set of figures shows the relationships between the channel width and the power and discharge voltage. As in the previous set, the width of the thruster has a major impact on the

amount of input power that can be used for useful output, as shown in figure 4.16. Additionally, the width also has an inverse effect on the discharge voltage similar to that in the first set, as figure 4.17 demonstrates.

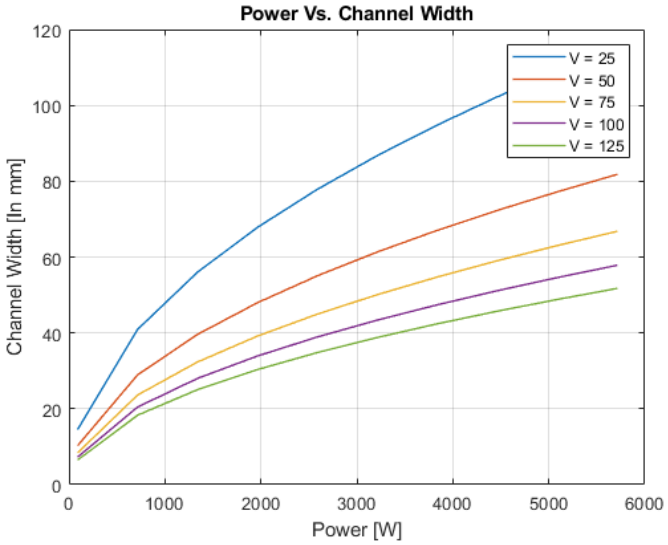

Figure 4.16 – Power-channel width relationship

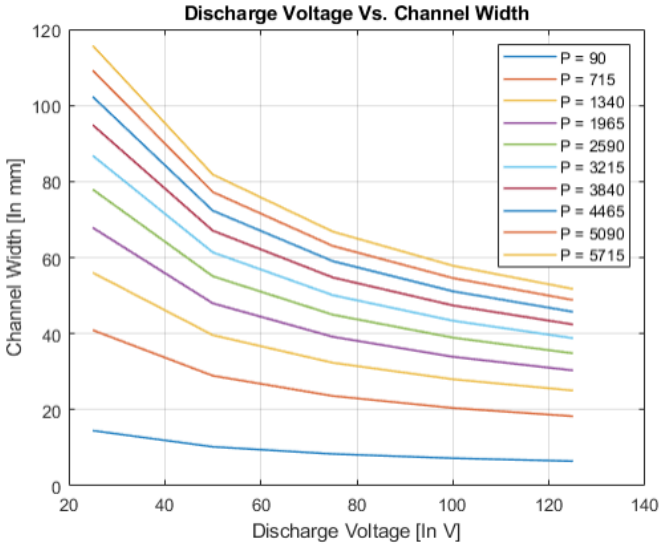

Figure 4.17 – Discharge voltage-channel width relationship

The third set of plots introduces the relationship of the input power to anode flow rate and the discharge voltage to the anode flow rate. It is shown that the anode flow rate tends to increase as the input power increases, as in figure 4.18. It is also shown that the anode flow rate tends to decrease with an increase of the discharge voltage, as in figure 4.19.

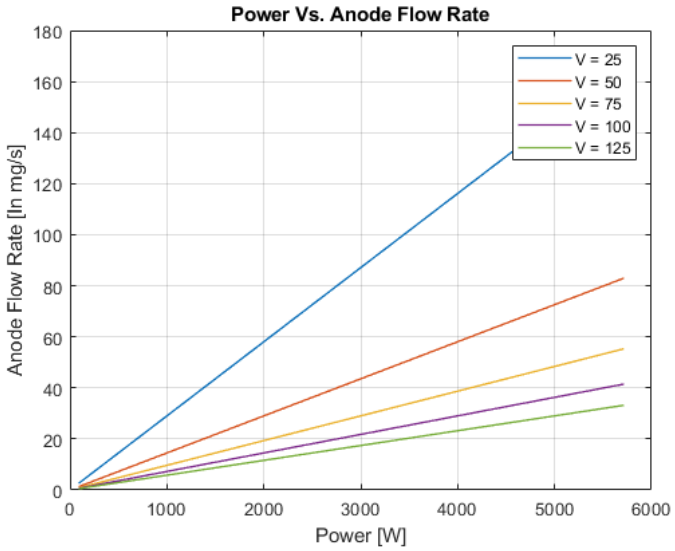

Figure 4.18 – Power-anode flow rate relationship

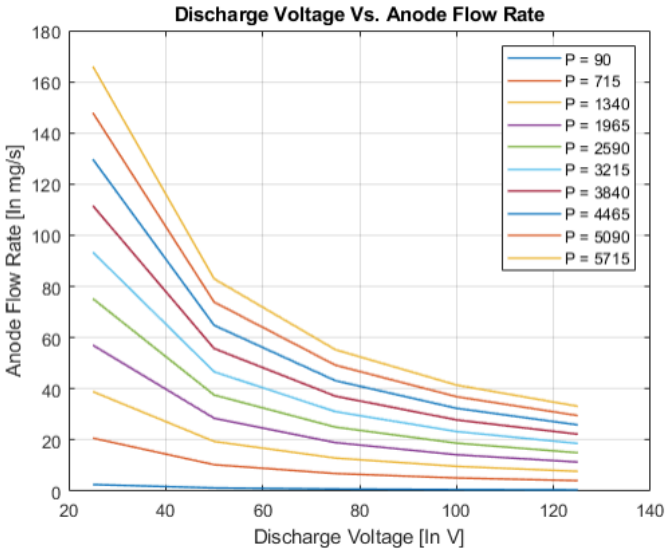

Figure 4.19 – Discharge voltage-anode flow rate relationship

The fourth set of figures compares the relationships between the thrust as it relates to the power and discharge voltage. Figure 4.20 demonstrates the trend between power and thrust. In this case, as the power increases, thrust generally increases and vice versa. Figure 4.21 on the other hand, shows an inverse relationship between the discharge voltage and thrust. In this case, as the discharge voltage decreases, the thrust tends to increase.

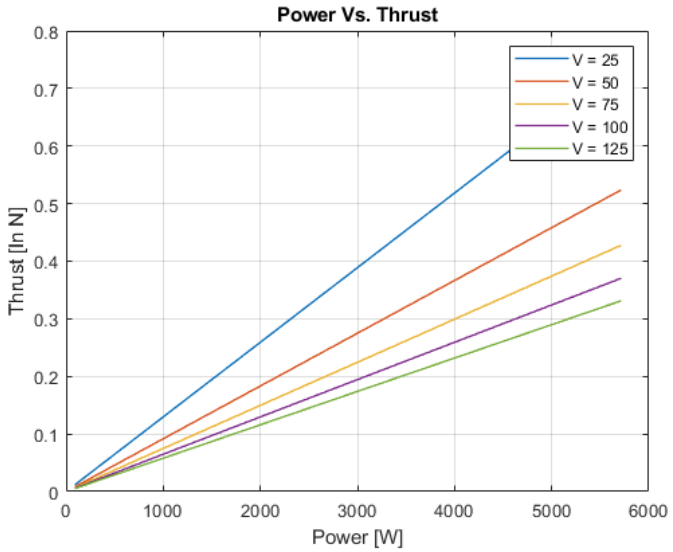

Figure 4.20 – Power-thrust relationship

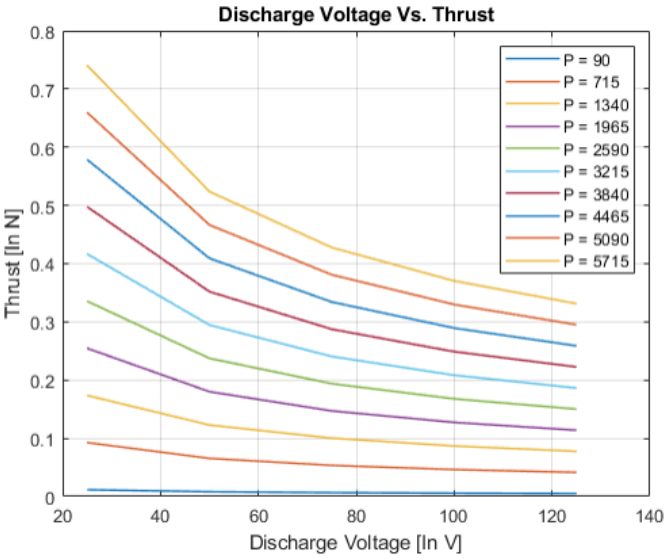

Figure 4.21 – Discharge voltage-thrust relationship

Set five presents the relationship between power and channel length as well as discharge voltage and channel length. In figure 4.22, it is shown that increasing the power in a thruster does not necessarily require an increase in width for optimal operation. However, as figure 4.23 shows, an increase in discharge voltage does require an increase in length for optimal performance.

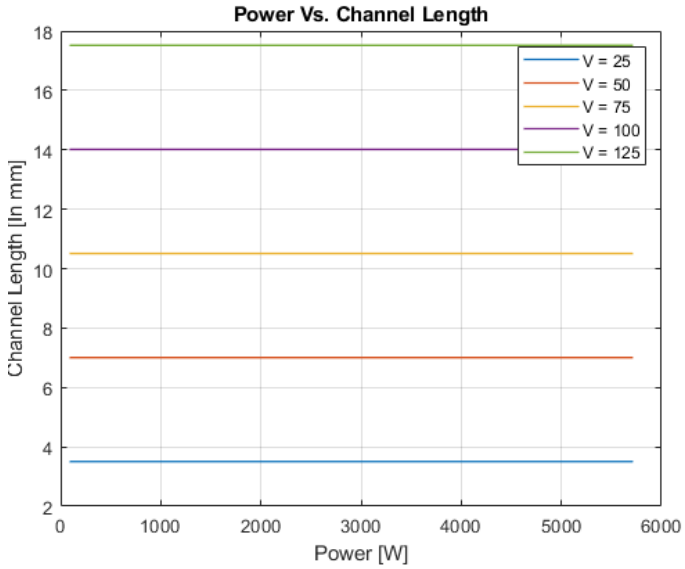

Figure 4.22 – Power-channel length relationship

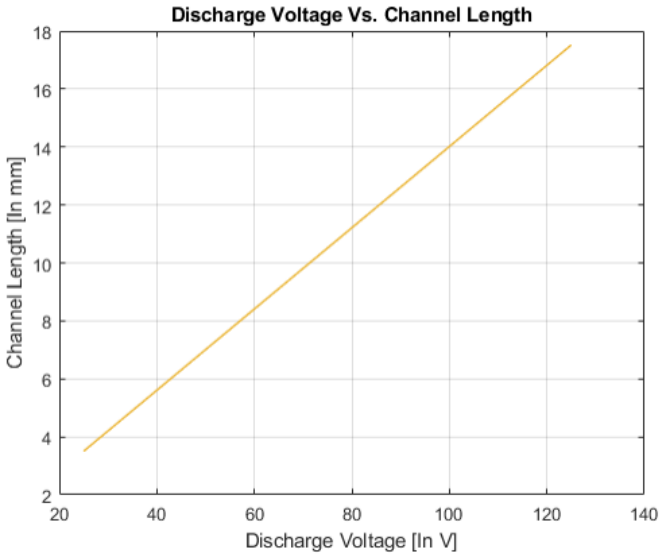

Figure 4.23 – Discharge voltage-channel length relationship

The final set of figures shows a constant relationship between power and specific impulse (figure 4.24) as well as a direct relationship between the discharge voltage and the specific impulse (figure 4.25). This relationship shows that as the discharge voltage increases, so does the specific impulse and vice versa.

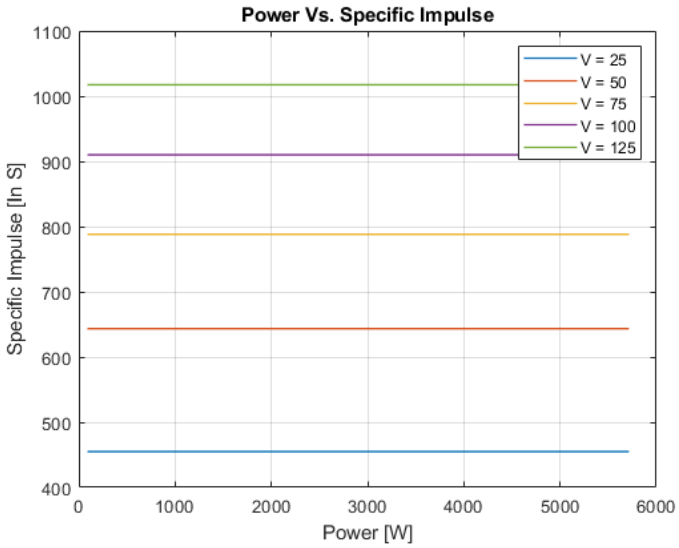

Figure 4.24 – Power-specific impulse relationship

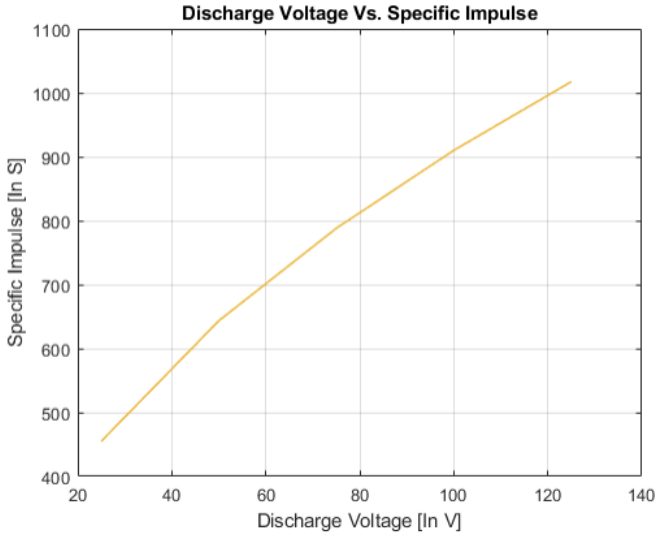

Figure 4.25 – Discharge voltage-specific impulse relationship

4.3.4 Analysis

The results achieved in this study demonstrate that varying the power magnitude as well as the discharge voltage has a direct effect on not only the dimensions of an optimal discharge channel of a hall-effect thruster but also its specific impulse and thrust. The following table shows a condensed overview of a select list of parameters that provide an optimized performance based on the preceding calculations.

Table 4 – Parameter overview

Discharge Voltage (V)	Power (W)	Channel Width (mm)	Channel Length (mm)	Channel Diameter (mm)	Thrust (N)	Specific Impulse (s)	Anode Flow Rate (mg/s)
25	90	14.52	3.5038	60	0.0117	454.99	2.61
50	360	20.53	7.01	84.85	0.033	643.46	5.23
25	500	34.22	3.50	141.42	0.065	454.99	14.52
50	780	30.22	7.01	124.90	0.072	643.46	11.33
25	2500	76.82	3.50	317.49	0.33	454.99	73.18
50	5000	76.6	7.01	316.23	0.4583	643.46	72.60

Chapter 5 - Numerical Algorithm

5.1 Introduction

One of the main thrust generation requirements of a hall-effect thruster relates to an axial mobility drop of the electrons due to the strong radial magnetic field present at the exit region of the thruster [18]. An electron azimuth drift is then experienced by this magnetic field which hinders the electrons' anode trajectory. Consequently, an axial electric field develops due to the increased resistance experienced by the electrons that is much stronger at the exit of the channel. This strong axial electric field forces the unmagnetized ions, which have larger masses, outward, creating thrust.

An important step in understanding how the interactions between the ions, electrons, and the electric field affect one another as well as the overall performance of the thruster is to fully understand the topology of the magnetic field. In general terms, the topology of the magnetic field in a hall-effect thruster is viewed in terms of intensity and location. During the design process of the thruster, the magnetic topology is generally implemented in such a way as to not allow for its non-radial component to interfere with the "magnetic lens" region of the thruster channel centerline [18].

The location of the magnetic lens has a direct effect on the life of a Hall thruster. When the operating temperature of the electrons is low, the magnetic lines are generally equipotential. This means that the thermal potential intensity is the same in all directions. This phenomenon translates to the magnetic field taking a radial configuration near the exit of the channel, which in turn, forces the accelerating ions to assume an axial configuration out of the thruster. In a mostly-axial ion configuration, the ions tend to hit the channel walls much less than they would if they were in a mostly-radial configuration. This cuts down on wall erosion and helps extend the life of the thruster.

In high electron operating temperatures, however, the opposite occurs. Equipotentiality is largely negligible, which forces the accelerating ions to take on a radial configuration as well as allows for the formation of sheaths of plasma near the channel wall. This combination of the accelerating ions bombarding a weakened wall due to the plasma sheaths leads to significant channel wall erosion, which reduces the life of the thruster.

One solution to remedy wall erosion while running the thruster at high temperatures or for long periods is through the use of magnetic shielding. Magnetic shielding is a technique in which the properties of plasma are exploited in such a way that reduces the energy of the accelerated ions hitting the walls. The way this technique works is through the modification of the magnetic field topology, where the magnetic field lines tangent to the wall penetrate to the anode, thus ensuring an equipotential configuration along those lines. This then leads to an electric field that is perpendicular to the wall at the channel exit, forcing minimal contact between the accelerated ions and the wall. Through this technique, wall erosion can be significantly reduced, thus increasing the life of a thruster even when running at high electron temperatures.

For the reasons discussed, magnetic shielding is an extremely important design requirement for long-term, interplanetary hall-thruster-powered missions. This, however, raises another challenge when designing a thruster for such missions. Generally, interplanetary missions and/or long-term missions require thrusters with high output, usually in the 10 kW and above range. Existing sizing parameters for such high output designs, however, would lead to thruster mass that significantly increases with an increasing discharge power. Therefore, optimization is a must.

One of the areas with major mass-saving and optimization potential is the magnetic circuit. Consisting of ferromagnetic and coil parts, the magnetic circuit can be configured to satisfy a wide range of performance requirements. The turns within the coils, for example, can be adjusted and optimized in such a way as to fulfill the desired topology of the magnetic field [18]. Various arrangements of the coils can be used to accomplish this. One such arrangement is the alignment of two coaxial inner and outer coils. Another arrangement involves an inner coil working in tandem with another set of coils that are positioned in column formation evenly on the outside of the thruster.

For hall thrusters with output power less than 1kW, magnetic coils are rarely used; instead, ferromagnets are used in their place. In such cases, the ferromagnets create magnetic field lines that rely on the low-reluctance path created by the ferromagnets, which then shape the thruster operation topology.

5.2 Methodology

5.2.1 Introduction

This portion of the project attempts to develop an optimization tool for the magnetically-shielded thruster's magnetic circuit. The development of this tool is split into two parts: Part one focuses on a computationally-efficient, but less accurate approximation approach for a mass-power Pareto analysis. Part two focuses on an exact solution approach to the optimization problem using a non-dominating sorting genetic algorithm (NSGA-II).

5.2.2 Part One: Magnetic Circuit Approximated Approach

The first step in the approximated approach is to lay out a list of the main circuit design parameters, as in figure 5.1, as well as to assess the characteristics of the magnetic circuit to make the optimization process simpler and more streamlined.

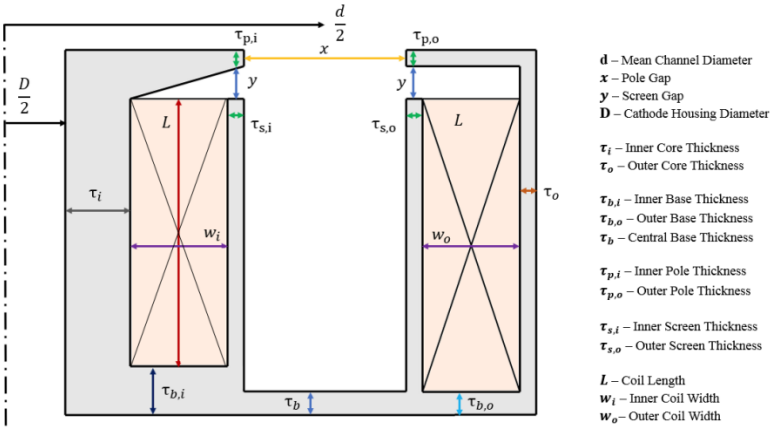

Figure 5.1 – Magnetic circuit parameters [18]

Using the magnetic circuit of the thruster as a guide, the equivalent electrical circuit can be constructed along with the fluxes and reluctances. The values of the reluctances depend on the parameters of the magnetic circuit. Using the values of the reluctances along with Kirchhoff's laws, the flux values can then be computed. The following set of equations are Kirchhoff's laws, where are derived from Maxwell's equations:

$$\int \nabla \cdot B \, dV = 0 \quad \rightarrow \quad \begin{matrix} \Phi = const \\ \sum \Phi_i = 0 \end{matrix} \tag{5.1}$$

$$\int \nabla \times B \cdot dS = \int \mu \, j \, dS \quad \rightarrow \quad \begin{matrix} \sum R_i \Phi_i = N_j I \\ R_i = \int \frac{dl}{\mu \cdot A} \end{matrix} \tag{5.2}$$

The gap reluctances in the circuit are then calculated by the following equation:

$$R = \int_o^s \frac{dl}{\mu_0 \mu_r \cdot A(l)} \tag{5.3}$$

Here *A(l)* is the relationship between the flux area and the coordinate *l*, where *l* is the path coordinate. One of the biggest challenges at this point is formulating a way to find the lengths of the gaps and the flux areas of the circuit. Although extremely difficult to calculate exact values, an approximation can be employed to yield sufficiently usable values, with considerations of the following assumptions:

- The flux tubes are three-dimensional
- Axisymmetry is present in the magnetic lines
- The flux tubes boundaries consist of straight lines and circular arcs

With the preceding assumptions in mind, an approximate geometric shape of the reluctances can now be developed as shown in figure 5.2. In the figure, the blue lines represent the *dl* integration path, while the green lines represent the *A(l)* integration path. Using equation 5.3, approximate reluctance values of the air gaps, as well as the ferromagnetic components, can now be achieved using numerical integration.

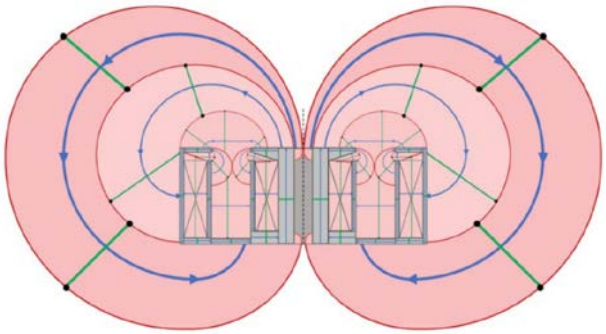

Figure 5.2 – Flux tube geometry [18]

Although calculating the values of most of the gaps is relatively straightforward, a problem begins to arise, however, when attempting to calculate the gap reluctance of the inner pole to outer pole screen due to them being modeled as parallel reluctances. In this case, a modified form of equation 5.3 is developed into the following form:

$$R_{IP-IS} = \left(\frac{1}{R_{IP-IS,1}} + \frac{1}{R_{IP-IS,2}}\right)^{-1} \tag{5.4}$$

Now that the needed formulas to solve for the different types of gap reluctances as well as the circuit components have been developed, a system of linear equations can now be constructed to solve for the unknown equivalent electrical circuit shown in figure 5.3. This electrical circuit gives an overview of the entirety of Hall thruster's magnetic circuit. Some of the components within it are The inner core (*IC*), inner pole (IP), inner screen (IS), inner base (IB), central base (B), outer base (OB), outer screen (OS), outer pole (OP), outer core (OC), inner core-to-inner screen air gap (IC-IS), inner pole-to-inner-screen air gap (IP-IS), inner screen-to-outer screen air gap (IS-OS), outer pole-to-outer screen air gap (OP-OS), outer core-to-outer screen air gap (OC-OS), inner pole-to-outer pole air gap (IP-OP), inner pole-to-outer core air gap (IP-OC) and inner core-to-outer base air gap (IC-OB) [18].

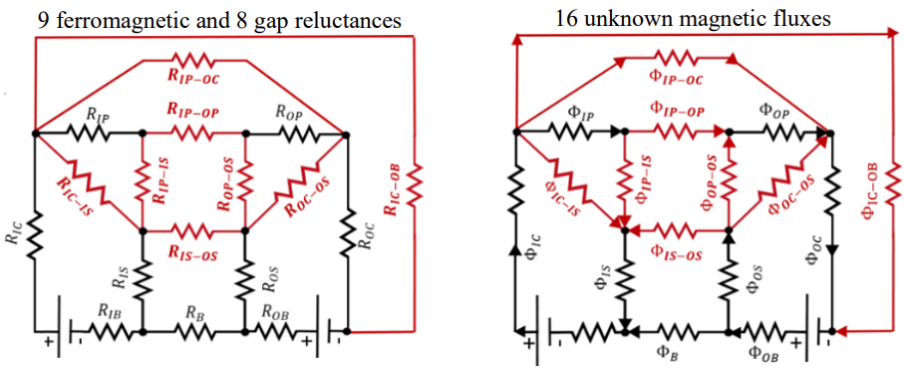

Figure 5.3 – Equivalent electrical circuit [18]

To assist in setting up the system of linear equations and to solve for the sixteen unknown magnetic fluxes, equation 5.5 is used. In this equation, an operation of integration is performed over the entirety of the circuit.

$$R_{IC-IS} = \frac{\left(\frac{1}{A_{IC}} + \frac{1}{A_{IS}}\right) \cdot L}{\mu_0 \cdot \mu_r \cdot \left[cosh\left(\sqrt{\frac{2\pi}{\mu_r \cdot k} \cdot \left(\frac{1}{A_{IC}} + \frac{1}{A_{IS}}\right)} \cdot L\right) - 1\right]} \sim \frac{k}{\mu_0 \cdot \pi \cdot L} = 2 \cdot \int_0^{w_i} \frac{dr}{\mu_0 \cdot A} \qquad (5.5)$$

where $k = ln\left(\frac{D}{2} + \tau_i + w_i\right) - ln\left(\frac{D}{2} + \tau_i\right)$

Using the preceding equation, the system of linear equations can now finally be set up into matrix form as shown in figure 5.4. The inputs in this system come from the magnetic circuit parameters (Figure 1). The output will be the sixteen unknown values. Those values will be used to determine each component's average magnetic field induction as well as the air gap.

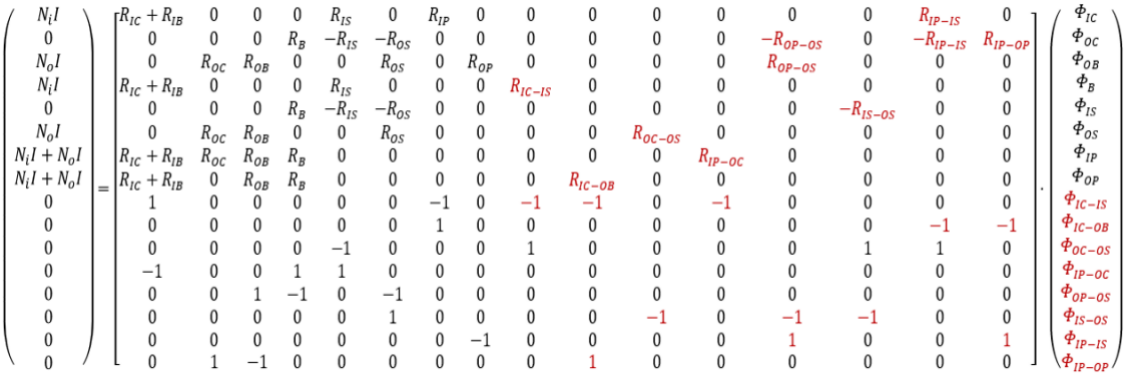

Figure 5.4 – Unknown matrices [18]

The aforementioned system is described as a lumped model. This model is nonlinear and is used to describe the magnetic circuit constraints that are imposed throughout the optimization process. One of the main purposes for the imposition of the constraints is to prevent magnetic saturation within the circuit as well as to make sure that the magnetic lens at the exit of the channel is symmetric. An additional purpose of the constraint imposition is that it allows for the acquisition of the magnetic peak value along the channel. The constraints can be described mathematically as:

$$max\left\{\frac{\Phi_{IC}}{A_{IC,min}};\frac{\Phi_{OC}}{A_{OC,min}};\ \frac{\Phi_{IC}}{A_{IB,min}};\frac{\Phi_{B}}{A_{B,min}};\frac{\Phi_{OB}}{A_{OB,min}};\ \frac{\Phi_{IS}}{A_{IS,min}};\frac{\Phi_{OS}}{A_{OS,min}};\frac{\Phi_{IP}}{A_{IP,min}};\frac{\Phi_{OP}}{A_{OP,min}}\right\} < \boldsymbol{B_{SAT}} \tag{5.6}$$

$$\Phi_{IP-IS} = \Phi_{OP-OS} \tag{5.7}$$

$$\frac{\Phi_{IP-OP}}{A_{IP-OP}} \geq \boldsymbol{B_{PEAK}} \tag{5.8}$$

Although efficient, one of the lumped model's shortcomings is that it is only capable of producing averaged magnetic field results over the flux tubes. This leads to the boundary areas of the tubes not being accurately accounted for in the calculations. This shortcoming also extends to the centerline magnetic field, where the intensity is not constant. In other words, a mean magnetic

field intensity is taken into account in the calculations, but in reality, much higher intensity can be present and should be accounted for to arrive at more accurate results.

Some of the constraints in the lumped model are purely geometrical and serve the purposes of adding robustness and allowing for field topology. The optimization is initialized by coupling the lumped model previously described to a Sequential Quadratic Programming algorithm, which then yields a function objective that can be described as follows:

$$OBJ = \frac{P}{P_{ref}} + \frac{M}{M_{ref}} \tag{5.9}$$

In the preceding formula, *M* is the value obtained from a geometric formulation of the circuit. *P* represents the power consumption of the magnets. This value can be calculated by using the cable lengths as well as the current input, considering the inner coil temperature to be 500°C and an outer coil temperature of 350°C. Now everything is ready to begin circuit power vs. power consumption Pareto analysis, which will be presented in the next section.

5.2.3 Part Two: Magnetic Circuit Exact Approach

The exact approach to the magnetic circuit optimization problem involves the utilization of a non-dominating sorting genetic algorithm. Due to the magnetic circuit optimization problem being multi-objective with conflicting parameters that are very difficult to optimize simultaneously, two approaches exact optimization approaches will be taken. The first approach involves treating all the required objectives as one objective by combining them all under one function. Depending on how such a function is defined, the objective outputs may or may not still conflict with one another. This is where some compromises and trade-offs need to be made for the final output to be of any significant use.

The second approach treats each objective as an individual and outputs a set of solutions called the Pareto set. In this approach, a concept called n-dimensional space domination is used. What this implies is that in an optimization problem where multiple parameters are to be

minimized, solution **A** is dominated by solution **B** if and only if the values of all objective functions corresponding to **B** are less than those for **A** [18]. This means that the solution of **B** is more accurate than those of **A**.

When this principle is applied to the hall thruster magnetic circuit, the conflicting objective could be the mass of the magnetic circuit and the coil power consumption. This relationship is conflicting because to increase the magnetic field, more coil needs to be added, which in turn, increases the mass of the system. Thus, power and mass need to be minimized as two separate objectives to achieve the best result possible under the given conditions. Therefore, the multi-objective non-dominating sorting genetic algorithm (NSGA-II) will be used to accomplish this.

The general idea behind how genetic algorithms work is that they randomly search a collection of possible solutions based on "mutation" and "selection," then they evolve into an optimum solution by iterating until convergence is achieved. The initial search is generally random and allows the algorithm to search for global rather than local solutions, which aids in arriving at the most usable solutions.

The specific idea behind how the algorithm works is that it starts with an initial population with an unspecified N_P members. Each member is a vector and is thought of as a chromosome. Randomly generated decision variables, or genes, occupy the same n-dimensional space as the vectors [18]. Mutation and crossover operators are randomly applied to the population and are assigned the variables N_m and N_c, respectively. Pairs of crossover operators within the population are then combined and are classified as "parents". They then begin to introduce new solutions, which are classified as "offspring". The offspring inherits the good "genes" or solutions from the "parents," which then helps to improve the accuracy of the resulting solution with each successive iteration [18].

The purpose of the crossover is to then introduce new members into the population that are somewhat different from the existing ones. By doing so, the diversity of the population is always maintained and feeds the algorithm sufficient global choices or options to pick from. As this is an iterative method, every member of the population is evaluated with every iteration. During the evaluation process, members are ranked using what is referred to as the "dominance rule." This rule sorts the members of the population based on their objective functions, which causes rank-

specific, non-dominated front divisions in the population. What this essentially means is that better solutions generally reside at fronts of lower ranks.

The aforementioned type of ranking is referred to as first-order ranking. Another type, second-order ranking, is also utilized and sorts members of the population based on equal fronts. In other words, fronts of equal ranks are grouped using relative crowd distance calculations. After sorting is complete, members or solutions that remain in non-crowded regions are considered more preferred than those in denser regions. This then marks the end of that iteration. The next iteration takes those preferred solutions, or members, and assigns *N* ranks to them from lowest to highest front, where the lowest front is referred to as *F1*. By doing this, the algorithm ensures that the preferred solutions are being kept track of while additional members are added with each successive iteration to maintain population diversity.

As the iterative process continues, *F1* begins to slowly approach the Pareto front, which signifies the end of the calculation. This point is generally met when either the number of predefined iterations is exhausted, or if convergence is achieved. Mathematically, this process is accomplished through a NAGA-II-based code developed in MATLAB, with an eventual goal of optimizing mass and power. A second objective involves optimizing the magnetic field topology. This is also done in MATLAB with the help of COMSOL Multiphysics.

The first phase of the optimization process deals with minimizing the mass of the circuit along with the coil power consumption while maintaining the target magnetic peak power at the centerline of the channel. Additionally, the optimization step should not increase the magnetic field intensity inside of the circuit as to not cause ferromagnetic saturation. If saturation occurs, considerable field line deviation will take place, which may cause further deficiencies in the topography. Furthermore, the magnetic field must be symmetrical to the channel line to allow maximum efficiency. Finally, two distinct objectives are used: coil power and mass. The rest of the parameters, namely the magnetic field peak value, saturation, and symmetry, will serve as the constraints [18] and are represented by formulas 5.10 and 5.11, where *f1* includes the peak value and saturation constraints, while *f2* includes the requirement of ensuring that channel centerline symmetry is obeyed.

$$f_1(X) = C_1 \left| \frac{B_p}{B_{peak}} - 1 \right|^2 + \left(max\left(0, \left(\frac{B_{max}}{B_{sat}} - 1\right)\right)\right)^2 \tag{5.10}$$

$$f_2(X) = \frac{1}{{B_p}^2}\left(C_2 \sum_{i=1}^{m} \left(\left(Bz_{R_i} - Bz_{L_i}\right)^2 + \left(Br_{R_i} - Br_{L_i}\right)^2 \right) + \int_{C.L} {B_z}^2 . dz \right) \tag{5.11}$$

In the preceding formulas, variables Bz_R, Br_R, $Bz_{Li,}$ and Br_L represent the magnetic field's axial and radial components along the centerline of the channel, respectively. C_1 and C_2 represent the weighting constants that need to be adjusted in the objective function. One of the main design constraints, namely the size of the channel, is implemented in the code in such a way that it has direct control over restricting decision variables along with other parameters for the sake of achieving the most optimal results possible for that specific case.

The components of the magnetic circuit in this phase of optimization are made up of the poles, screens, coaxial coils, and the base. A geometric overview of this setup is shown in figure 5.5. As shown in the figure, the dimensions of the components, as well as the coil current, are all presented as an X decision vector. This helps in constraining some of the parameters to maintain the dimensions as the optimization progresses. Due to this optimization problem being multi-objective, no single solution is optimal.

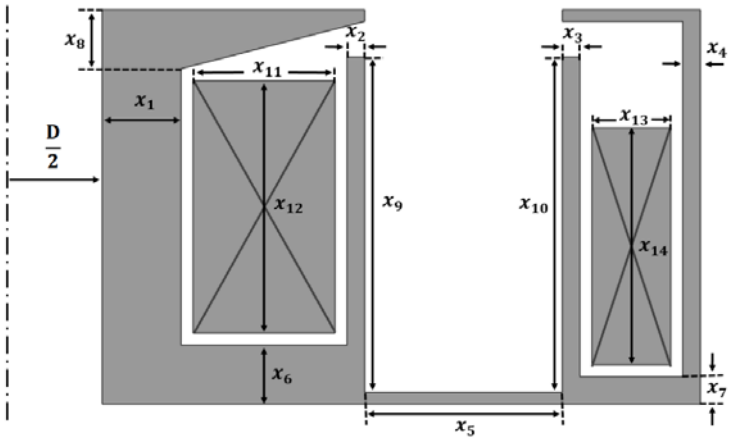

Figure 5.5 – Circuit configuration [18]

The second phase of the optimization process focuses on introducing magnetic shielding by changing the topology of the magnetic field. This is to be accomplished while still maintaining the parametric constraints previously set. Thus, the modification of the topology will involve minimal changes to the circuit geometry as well as to the coils. Additionally, minor current modifications will be made, which along with the other changes will be contained under a decision vector called *Y*.

The magnetic field topology is superimposed on the model using a point set that is defined in specific regions where the field lines are to be aligned with the target magnetic field topology. This point set is created to be a function of the dimensions of the channel. By doing so, it will be possible to apply this same topology to other hall thrusters with different power outputs and/or dimensions. Due to the magnitude of the magnetic field being set in phase one, however, only the field topology will be modified as an objective function in this phase. This is especially true since the power output has already been chosen [18]. The target topology that is based on the set of points derived from the objective function can be expressed by the following formula:

$$f_1(Y) = \sum_{i=1}^{n} \left(\left(\frac{\frac{W}{L}}{\frac{W_{ref}}{L_{ref}}} \right) \left(\frac{Br_i}{Bz_i} \right) - \frac{Br_{ref}{}_i}{Bz_{ref}{}_i} \right)^2 \tag{5.12}$$

Where the aspect ratio scaling, $\frac{W}{W_{ref}}$ and $\frac{L}{L_{ref}}$ of the reference thruster is incorporated into *f1(Y)*.

Control point distribution is designed in such a way that places points of relative higher importance ahead of those with relative lower importance to the topology at different regions. This helps ensure that the “grazing line” can penetrate deep into the channel, which is one of the main requirements for magnetic shielding due to this line having high potential and low temperature. Changes in the magnitude of the grazing line along the centerline are an indicator of the proximity changes between the grazing line and the anode [18]. The changes in magnitude can be used as a function of how much shielding is needed.

A final consideration for this phase is to ensure that the required peak magnetic field along the centerline is sufficiently higher than what is required for thruster operation. Otherwise, other systems will begin to fail. The final objective constraints are presented in formulas 5.13 and 5.14.

$$f_1(Y) = \sum_{i=1}^{n} \left(\left(\frac{\frac{W}{L}}{\frac{W_{ref}}{L_{ref}}} \right) \left(\frac{Br_i}{Bz_i} \right) - \frac{Br_{ref_i}}{Bz_{ref_i}} \right)^2 \tag{5.13}$$

$$f_1(Y) = \sum_{i=1}^{n} \left(\left(\frac{\frac{W}{L}}{\frac{W_{ref}}{L_{ref}}} \right) \left(\frac{Br_i}{Bz_i} \right) - \frac{Br_{ref_i}}{Bz_{ref_i}} \right)^2 \tag{5.14}$$

5.3 Results

5.3.1 Introduction

This section compiles the sets of optimization results achieved from the calculations presented in the previous sections. The results are based on a 5-kW Hall thruster with voltages in the 300-450 range with varying channel dimensions. Four cases are being investigated. The power in cases A and B are kept constant; the voltages are set at 300V for case A and 450V for case B; and the dimensions for both cases are kept free. In cases C and D, both the power and voltages are kept constant at 5kW and 450V, respectively, while the channel dimensions vary from 5.5 for case C to 6.5 for case D. These requirements are set for the first phase of the optimization.

Using the aforementioned cases A to D as the values to be used for the second phase of the optimization, the resulting value of the optimized magnetic shielding is $1.2B_{peak}$ [18], whereby using the temperatures and the resistance of the coil cables, the power consumption of the coils is calculated. Additionally, the outer and inner coils have the same currents. Optimization parameters and Pareto front trends obtained from the exact and approximate approaches are presented in the following sections.

5.3.2 Optimized Geometric Circuit

The results of the optimized geometry are presented in the following series of figures. Figures 5.6 to 5.9 show the approximate solutions of the relationship between the power and the circuit mass for cases A, B, C, and D. The circles in each plot represent all the points where all the optimized geometries reside with respect to constraint requirements. Figures 5.10 to 5.13 show the same relationships as figures 5.6 to 5.9, but for the exact solutions.

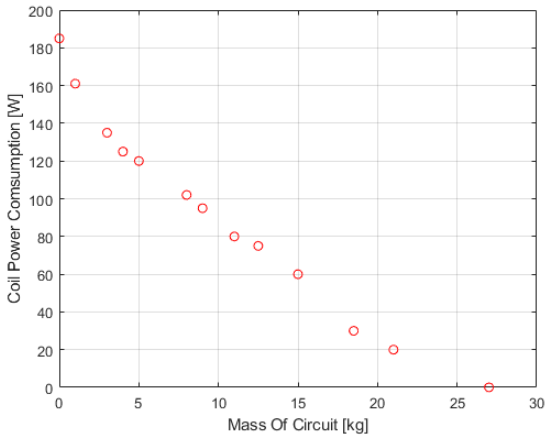

Figure 5.6 – Case A approximate

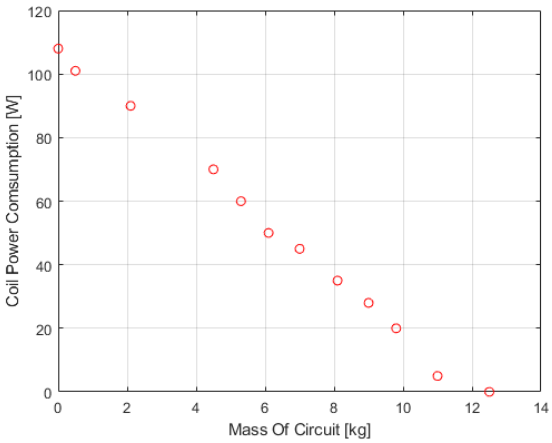

Figure 5.7 – Case B approximate

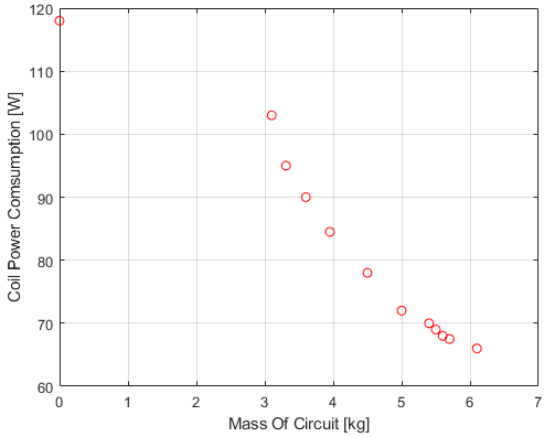

Figure 5.8 – Case C approximate

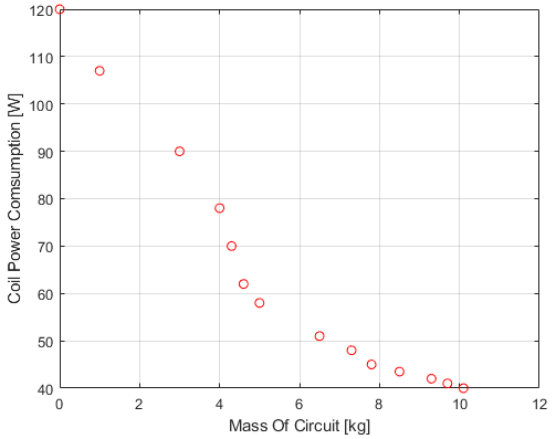

Figure 5.9 – Case D approximate

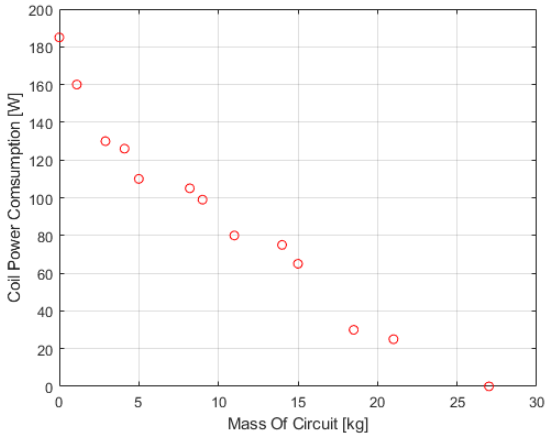

Figure 5.10 – Case A exact

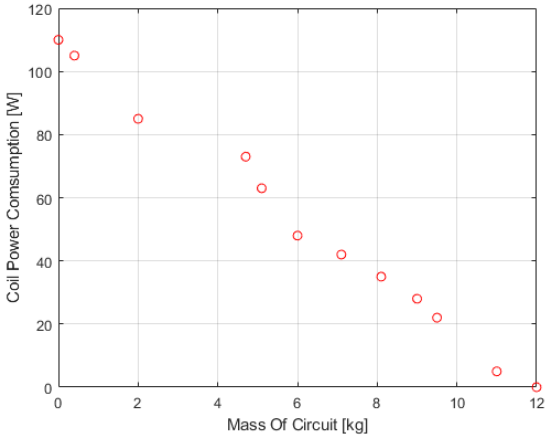

Figure 5.11 – Case B exact

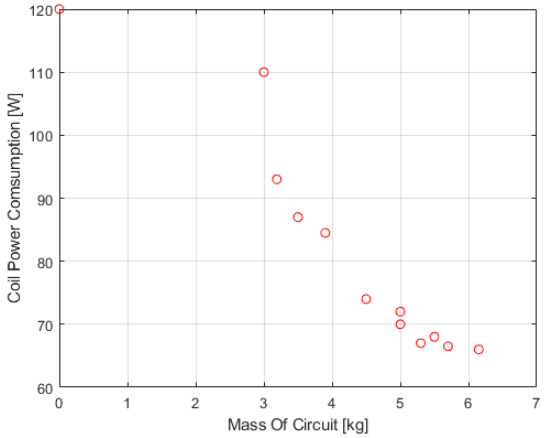

Figure 5.12 – Case C exact

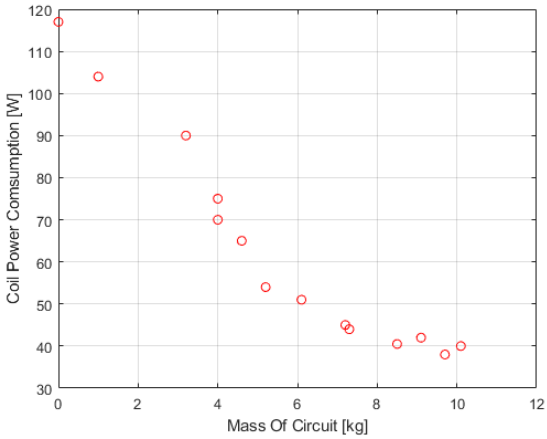

Figure 5.13 – Case D exact

As evident by the two sets of plots, the approximate solutions are very close to the exact solutions. This shows that the approximate method used for the circuit model is of acceptable accuracy. The trends for both sets show that as the mass of the coil circuit increases, the coil power consumption decreases. This behavior is per the hall thruster scaling laws [18]. Similar trends apply to the geometric trends that involve the channel diameter and width along with the mass and power of the system, as shown in the following series of figures.

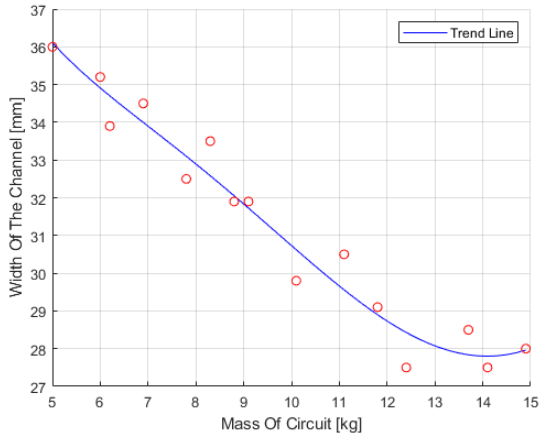

Figure 5.14 – Width vs. mass case A

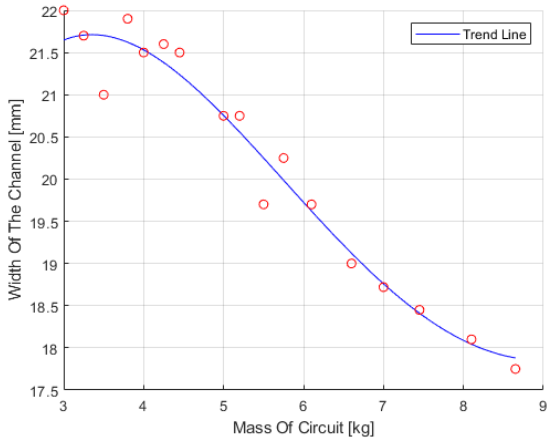

Figure 5.15 – Width vs. mass case B

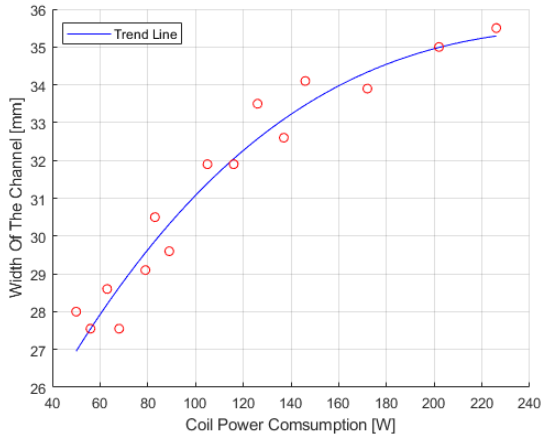

Figure 5.16 – Width vs. power case A

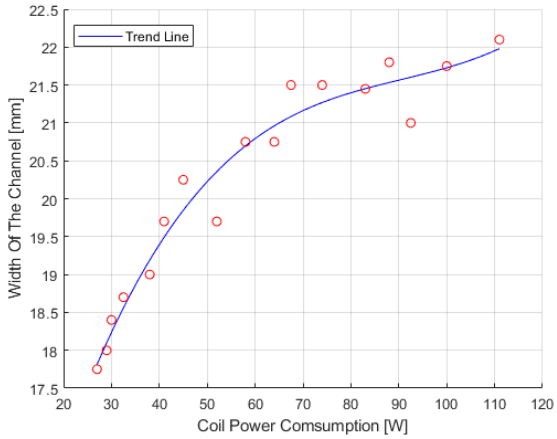

Figure 5.17 – Width vs. power case B

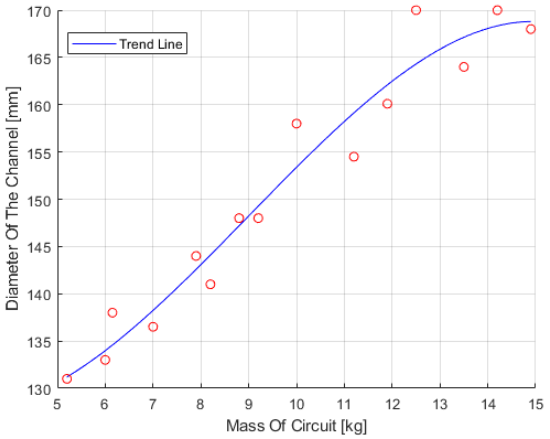

Figure 5.18 – Diameter vs. mass case A

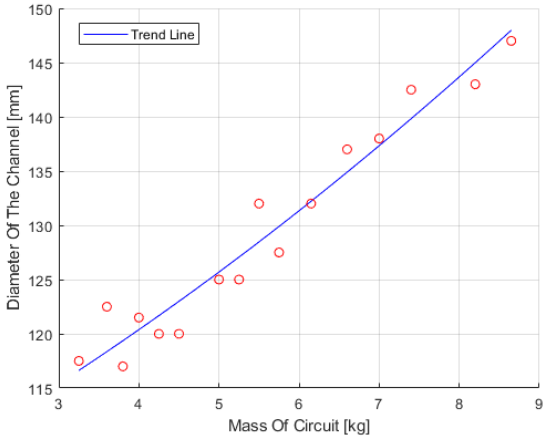

Figure 5.19 – Diameter vs. mass case B

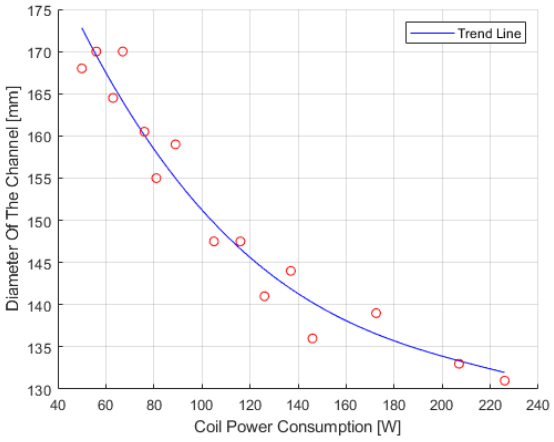

Figure 5.20 – Diameter vs. power case A

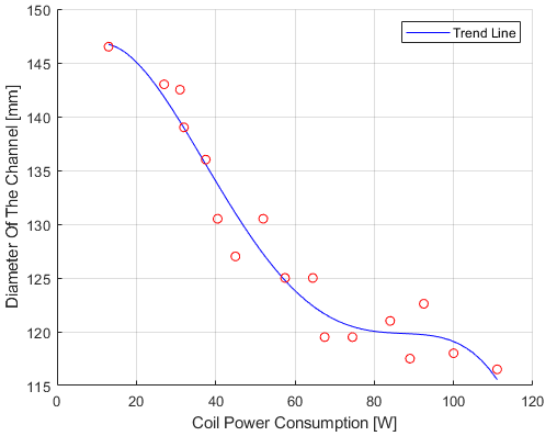

Figure 5.21 – Diameter vs. power case B

Like the previous series of trends shows, when the mean diameter and channel width ratios decrease, the Pareto front for the mass ratio becomes smaller. However, as the diameter and channel ratios increase, the Pareto front power ratio becomes larger. Such trends are in line with those in figures 5.6 to 5.13. Additionally, the resulting trends in figures 5.14 to 5.21 show that when a fixed channel area is widened (when the diameter is decreased), mass is favored over power. When the diameter is increased, however, the coil power consumption decreases, but at the cost of an increase in the circuit mass.

The next series of figures show the optimized current against the coil number of turns for cases A, B, C, and D. As the trends show, by increasing the number of coil turns, a reduction in current for a fixed value of magnetic field peak takes place [18].

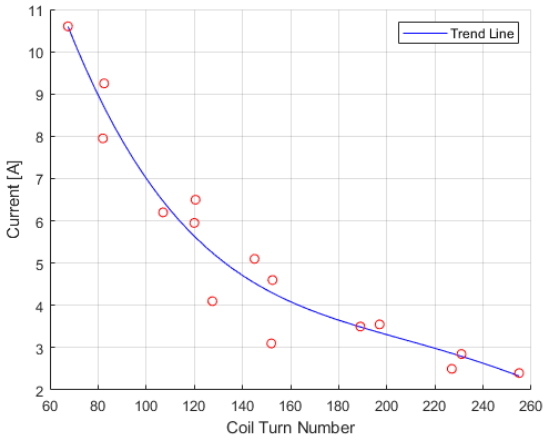

Figure 5.22 – Turns vs. current case A

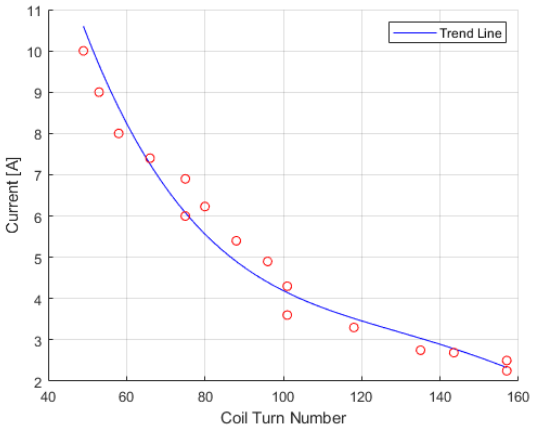

Figure 5.23 – Turns vs. current case B

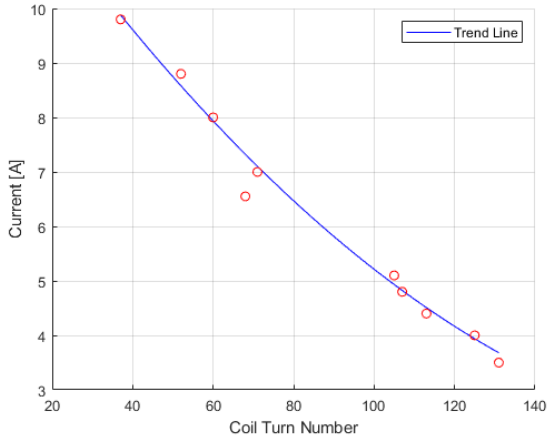

Figure 5.24 – Turns vs. current case C

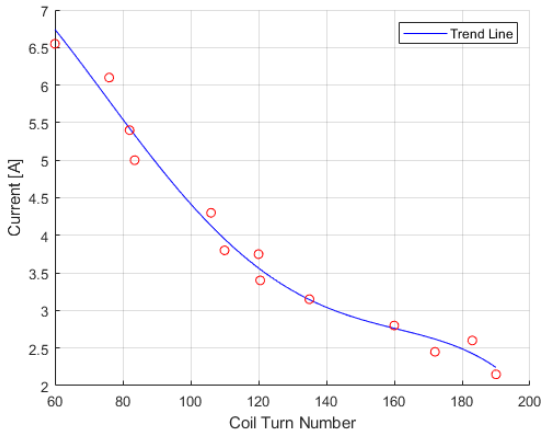

Figure 5.25 – Turns vs. current case D

5.3.3 Optimized Magnetic Topology

The topology in this phase is based on one of the design cases from the previous section. Case A is chosen due to it being halfway between the mass and power extremes of the rest of the cases, with a mass of 8 kg and power of 130 W. Here the magnetic topology satisfies the required B_{peak} magnetic shielding, with the output being a set of values that satisfies the minimum objective functions values required. The following figure shows the full topology of the magnetic field of Case A.

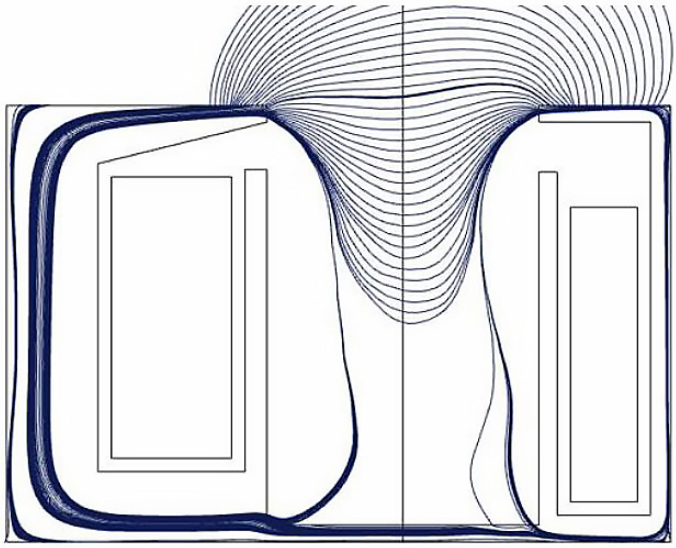

Figure 5.26 – Magnetic topology [18]

Utilizing the same process used for Case A, a set of solutions for the rest of the cases can be easily achieved. Using those solutions, it can then be determined which case provides a minimum value of the objective function that satisfies the given constraints. That case would then be considered to be the most optimized, with the discrepancy error between the cases can be described by the following formula:

$$f(Y) = \frac{1}{N}\sum_{i=1}^{n}\left(\frac{\left(\frac{\frac{W}{L}}{\frac{W_{ref}}{L_{ref}}}\right)\left(\frac{Br_i}{Bz_i}\right)}{\frac{Br_{ref_i}}{Bz_{ref_i}}} - 1\right)^2 \tag{5.15}$$

5.4 Benchmark

This section presents a series of figures comparing the calculated results to previously published benchmark data. Some of the comparisons covered include the mass of the coils in the magnetic circuit versus their power consumption; the channel width versus circuit mass and coil power consumption; channel diameter versus circuit mass and power consumption; coil turn number versus the current produced.

This section aims to highlight the similarities between the solutions achieved by this work and those achieved by the benchmark data. This benchmark analysis step is important in checking whether or not the results achieved are in line with the published work, as recreating a published work with known parameters and values helps set a baseline for further improvements. With this in mind, the above sets of plots show that the results obtained follow closely the results of the benchmark, with only minor deviations in the mass versus power consumption for cases A, B, C, and D. This deviation may be the result to an undetermined error in the code.

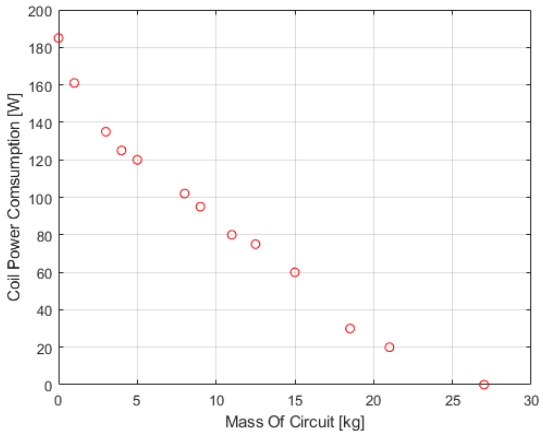

Figure 5.27 – Mass vs. power case A

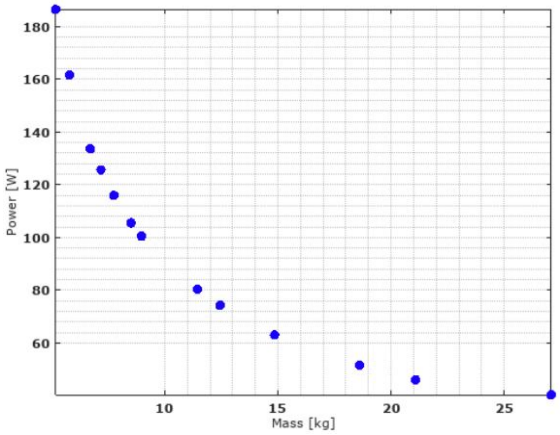

Figure 5.28 – Mass vs. power case A benchmark

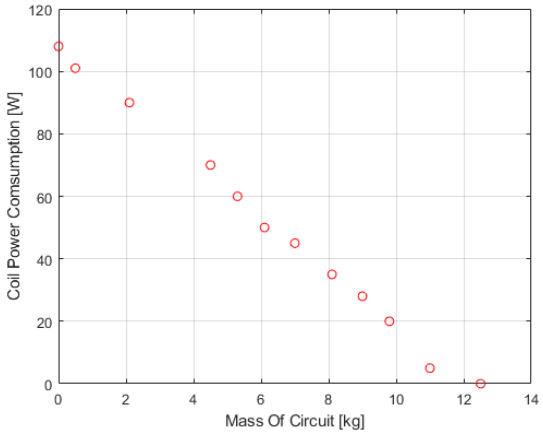

Figure 5.29 – Mass vs. power case B

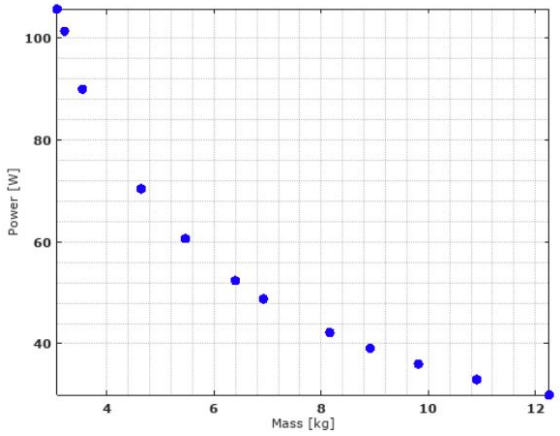

Figure 5.30 – Mass vs. power case B benchmark

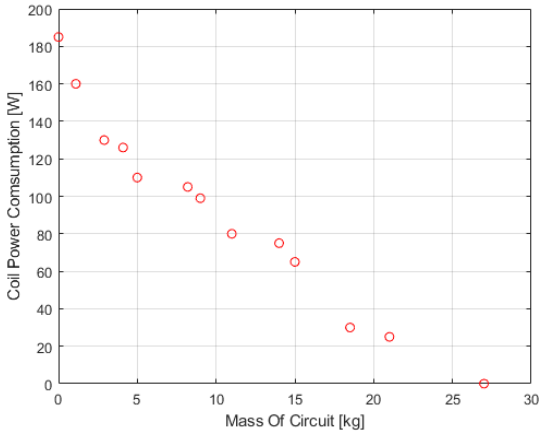

Figure 5.31 – Mass vs. power case C

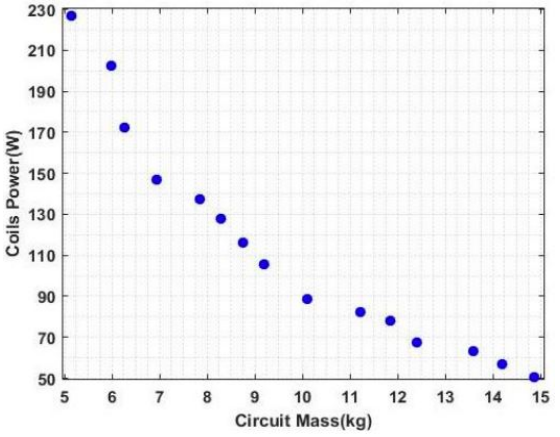

Figure 5.32 – Mass vs. power case C benchmark

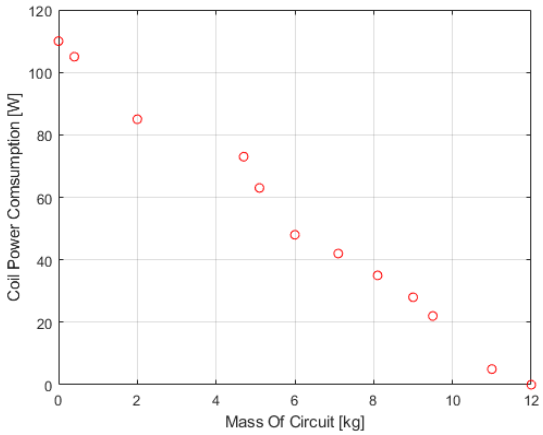

Figure 5.33 – Mass vs. power case D

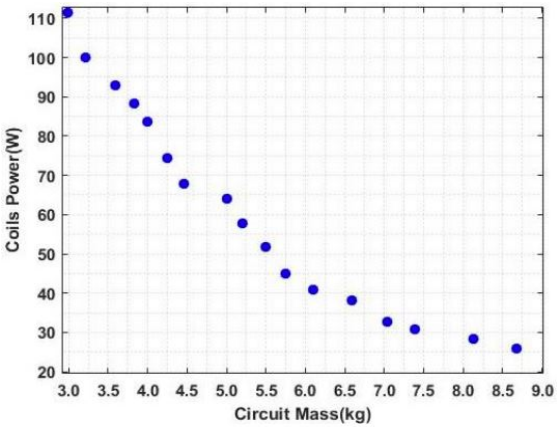

Figure 5.34 – Mass vs. power case D benchmark

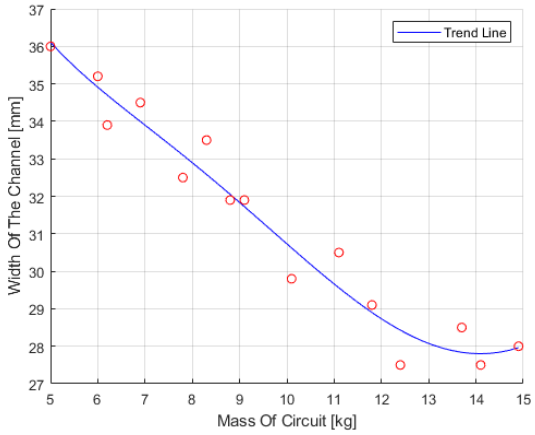

Figure 5.35 – Mass vs. width case A

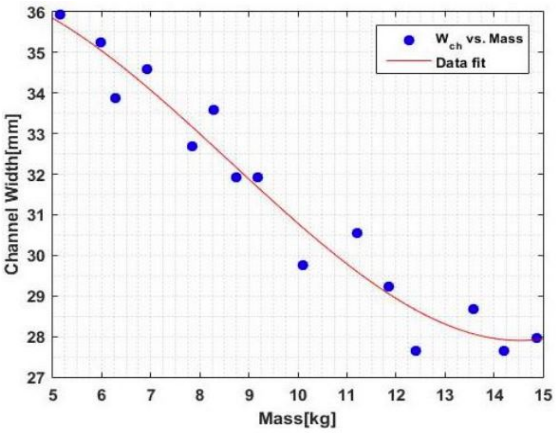

Figure 5.36 – Mass vs. width case A benchmark

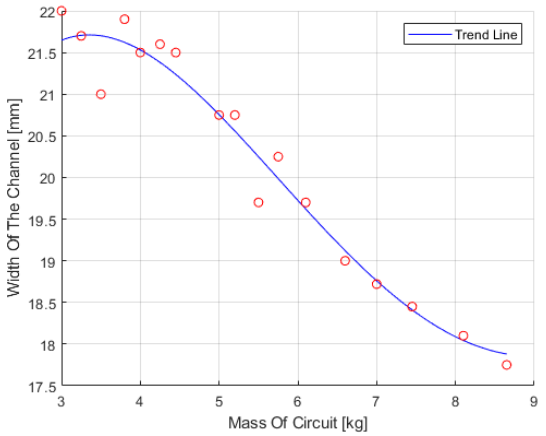

Figure 5.37 – Mass vs. width case B

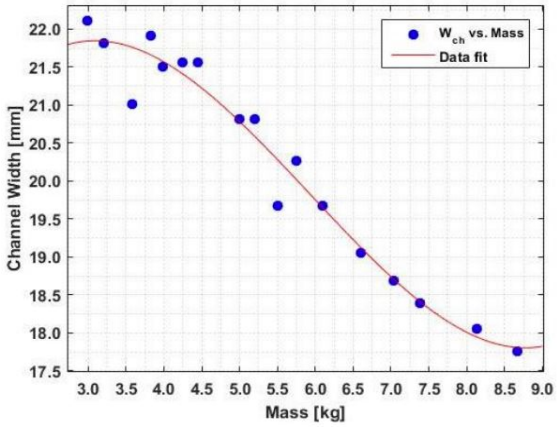

Figure 5.38 – Mass vs. width case B benchmark

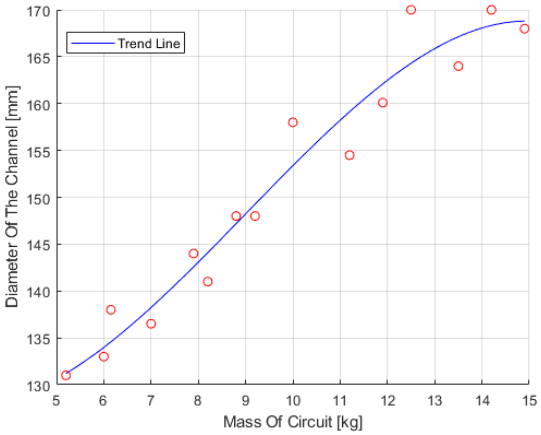

Figure 5.39 – Mass vs. diameter case A

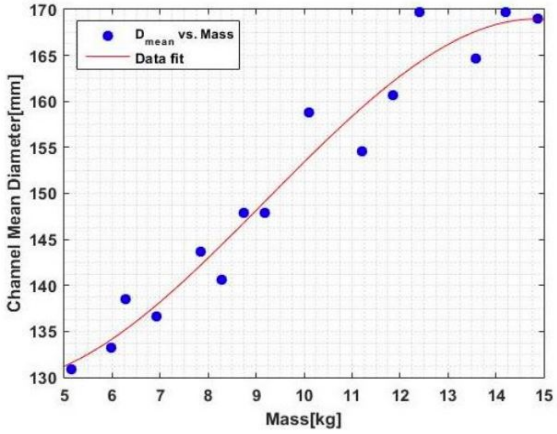

Figure 5.40 – Mass vs. diameter case A benchmark

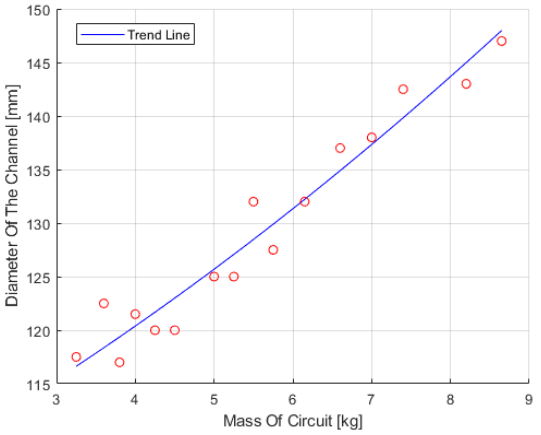

Figure 5.41 – Mass vs. diameter case B

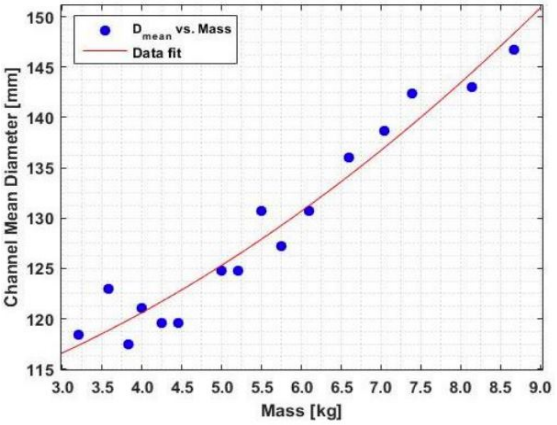

Figure 5.42 – Mass vs. diameter case B benchmark

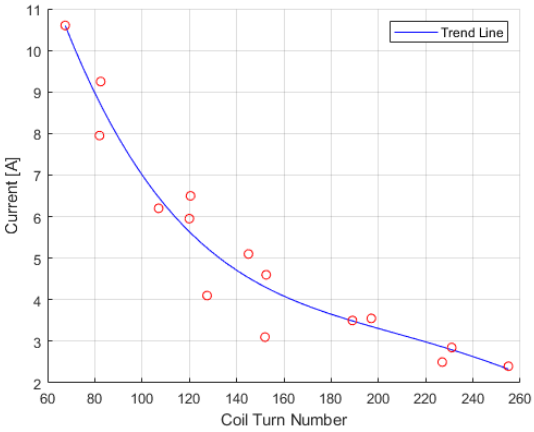

Figure 5.43 – Coil turns vs. current case A

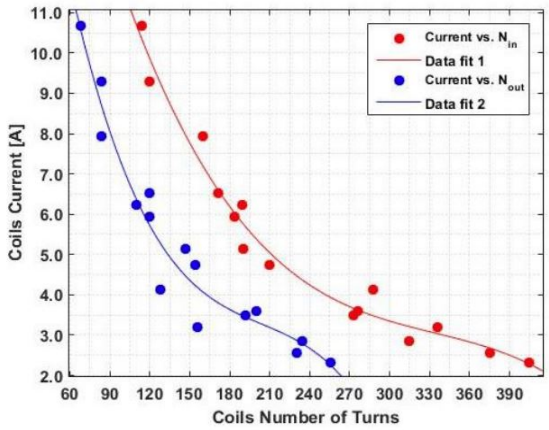

Figure 5.44 – Coil turns vs. current case A benchmark

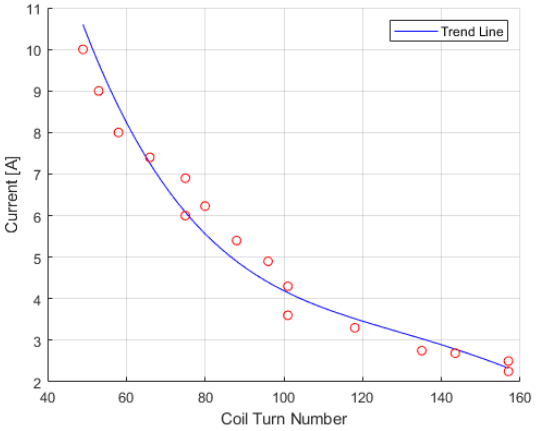

Figure 5.45 – Coil turns vs. current case B

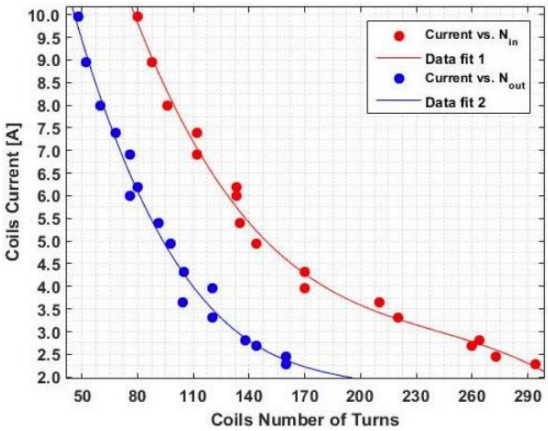

Figure 5.46 – Coil turns vs. current case B benchmark

Chapter 6 – Conclusion

6.1 Discussion

The work presented in this study shows the optimization results of various components on a hall-effect thruster. It shows the relationships that different parameters have on the mass of the magnetic circuit, and by extension, the whole system. An analytical model of the thruster's magnetic circuit was built to efficiently approximate some of the circuit's characteristics. The method used to produce this model was through discretizing the fluxes and reluctances of the magnetic circuit, followed by the creation of an equivalent electrical circuit. This approximate method was then coupled with an algorithm to produce accurate data at every thruster power level as well as at different channel configurations.

With the help of the NAGA-II algorithm presented in this paper, an effective magnetic field topology was produced and can easily be applied to a variety of hall thrusters of different outputs and sizes. In addition to the topology, the algorithm was also able to produce reasonably accurate optimization trends that relate coil power withdrawal to channel width, coil mass to channel width, coil mass to channel diameter, and coil power withdrawal to channel diameter along with other useful trends. It is then appropriate to conclude that adjusting the relationships in those trends can have a direct impact on the overall performance of the thruster in general, and the thrust produced in particular.

6.2 Future Work

Although the optimizations performed in this study are sufficient for general hall-effect thruster applications, some applications that require extremely long operation times do require a much more robust magnetic shielding. This may be possible when further developments into improvements of electrical circuit discretization accuracy

References

[1] Goebel, D. M., and Katz, I., *Fundamentals of electric propulsion ion and Hall thrusters*, Wiley, New Jersey, 2008.

[2] Fu, M., Zhang, D., and Li, T., "New Electrical Power Supply System for All-Electric Propulsion Spacecraft," *IEEE Transactions on Aerospace and Electronic Systems*, Vol. 53, 2017, pp. 2157–2166. doi: 10.1109/taes.2017.2683638

[3] Frieman, J. D., Peterson, P. Y., Gilland, J. H., Kamhawi, H., Williams, G., Herman, D. A., and Hofer, R. R., "Long Duration Wear Test of the NASA HERMeS Hall Thruster," *2018 Joint Propulsion Conference*, 2018. doi: 10.2514/6.2018-4645.c1

[4] Fan, H., Li, H., Ding, Y., Wei, L., and Yu, D., "Effects of the peak magnetic field position on Hall thruster discharge characteristics," *Advances in Space Research*, No. 66, 2020, pp. 2024–2034. doi: 10.1016/j.asr.2020.06.036

[5] Ding, Y., Sun, H., Li, P., Wei, L., Xu, Y., Peng, W., Su, H., and Yu, D., "Influence of hollow anode position on the performance of a hall-effect thruster with double-peak magnetic field," *Vacuum*, Vol. 143, 2017, pp. 251–261. doi: 10.1016/j.vacuum.2017.06.030

[6] Tahara, H., Imanaka, K., and Yuge, S., "Effects of channel wall material on thrust performance and plasma characteristics of Hall-effect thrusters," *Vacuum*, Vol. 80, 2006, pp. 1216–1222. doi: 10.1016/j.vacuum.2006.01.049

[7] Kurzyna, J., Jakubczak, M., Szelecka, A., and Dannenmayer, K., "Performance tests of IPPLMs krypton Hall thruster," *Laser and Particle Beams*, Vol. 36, 2018, pp. 105–114. doi: 10.1017/s0263034618000046

[8] Turan, N., Korkmaz, O., and Celik, M., "Investigation of the effect of hollow cathode neutralizer location on hall effect thruster efficiency," *2015 7th International Conference on Recent Advances in Space Technologies (RAST)*, 2015. doi: 10.1109/rast.2015.7208414

[9] Li, H., Wu, Y., Ding, M., Ding, Y., Wei, L., Yu, D., and Wang, X., "Discharge characteristics of a Kilowatt Hall effect thruster with a variable channel," *Vacuum*, Vol. 153, 2018, pp. 291–299. doi: 10.1016/j.vacuum.2018.04.035

[10] Cao, S., Wang, X., Ren, J., Ouyang, N., Zhang, G., Zhang, Z., and Tang, H., “Performance and plume evolutions during the lifetime test of a Hall-effect thruster,” *Acta Astronautica*, Vol. 170, 2020, pp. 509–520. doi: 10.1016/j.actaastro.2019.12.036

[11] Khmelevskoi, I. A., and Tomilin, D. A., “Parametric Study of Two Stable Forms of Discharge Burning in a Hall-Effect Thruster,” *Technical Physics*, Vol. 64, 2019, pp. 1283–1289. doi: 10.1134/s1063784219090068

[12] Moshnyakov, A., and Mikhaylov, M., “Power processing unit for hall-effect thrusters on ‘Meteor-M №3 spacecraf,’” *MATEC Web of Conferences*, Vol. 48, 2016, pp. 01007. doi: 10.1051/matecconf/20164801007

[13] Koo, J. W., and Boyd, I. D., “Computational model of a Hall thruster,” *Computer Physics Communications*, Vol. 164, 2004, pp. 442–447. doi: 10.1016/j.cpc.2004.06.058

[14] Li, H., Ning, Z., and Yu, D., “Hall thruster with grooved walls,” *Journal of Applied Physics*, Vol. 113, 2013, pp. 083303. doi: 10.1063/1.4793561

[15] Wendt, J. F., and Anderson, J. D., Computational fluid dynamics: an introduction, Berlin: Springer, 2010.

[16] Domínguez-Vázquez, A., Taccogna, F., Fajardo, P., & Ahedo, E. (2019). “Parametric Study of the Radial Plasma-Wall Interaction in a Hall Thruster,” *Journal of Physics D: Applied Physics*, 52(47), 474003. https://doi.org/10.1088/1361-6463/ab3c7b

[17] Domínguez-Vázquez, A., Taccogna, F., & Ahedo, E. (2018). “Particle modeling of radial electron dynamics in a controlled discharge of a Hall thruster,” *Plasma Sources Science and Technology*, *27*(6), 064006. https://doi.org/10.1088/1361-6595/aac968

[18] Reza, M., Ferrato, E., Faraji, F., & Andreussi, T. (2019). “Magnetic Circuit Optimization for Hall Thrusters Design,” *International Electric Propulsion Conference*, 1–22. Retrieved from https://www.researchgate.net/publication/355037699_Magnetic_Circuit_Optimization_for_Hall_Thrusters_Design.

Appendices

Appendix A – Parametric Study MATLAB Codes

```
clear all;
clc;

% This code plot the Power Vs. Channel Diameter and Discharge Voltage
 Vs.
% Channel Diameter.

Ud = 25:25:125; % Discharge Voltage
P = 90:625:6250; % 100:100:500 % Watt
Loss = 4 ; % Wall Loss In Percent
Eff = 0.9 ; % Inonizaation Efficiency
nn = 1.2 * 10^19; % m^-3 (Atomic number density)
alpha = 0.9 ; %(Propellant conversion efficiency)
%
 ================================================================================
dm = sqrt(P'./ (1000 .*Ud)); % [m]
dmm = dm *1000; % [mm]
figure,
plot(P,dmm,'LineWidth',1);
title('Power Vs. Channel Diameter');
legend('V = 25', 'V = 50','V = 75', 'V = 100','V = 125');
xlabel('Power [W]');
ylabel('Channel Diamter [In mm]');
grid on;
figure,
plot(Ud,dmm,'LineWidth',1);
title('Discharge Voltage Vs. Channel Diameter');
legend('P = 90', 'P = 715','P = 1340','P = 1965','P = 2590','P =
 3215','P = 3840','P = 4465','P = 5090','P = 5715');
xlabel('Discharge Voltage [In V]');
ylabel('Channel Diamter [In mm]');
grid on;
```

```
clear all;
clc;

% This code plots the Power Vs. Channel Width and Discharge Voltage
 Vs.
% Channel Width.

Ud = 25:25:125; % Discharge Voltage
P = 90:625:6250; % 100:100:500 % Watt
Loss = 4 ; % Wall Loss In Percent
Eff = 0.9 ; % Inonizaation Efficiency
nn = 1.2 * 10^19; % m^-3 (Atomic number density)
alpha = 0.9 ; %(Propellant conversion efficiency)
%
 ================================================================================
dm = sqrt(P'./ (1000 .*Ud)); % [m]
dmm = dm *1000; % [mm]
wmm = 0.242 * dmm; %[mm]
wm = wmm/1000; %[m]
figure,
plot(P,wmm,'LineWidth',1);
title('Power Vs. Channel Width');
legend('V = 25', 'V = 50','V = 75', 'V = 100','V = 125');
xlabel('Power [W]');
ylabel('Channel Width [In mm]');
grid on;
figure,
plot(Ud,wmm,'LineWidth',1);
title('Discharge Voltage Vs. Channel Width');
legend('P = 90', 'P = 715','P = 1340','P = 1965','P = 2590','P =
 3215','P = 3840','P = 4465','P = 5090','P = 5715');
xlabel('Discharge Voltage [In V]');
ylabel('Channel Width [In mm]');
grid on;
```

```
clear all;
clc;

% This code plots the Power Vs. Anode flow rate and Discharge Voltage
 Vs.
% Anode flow rate.

Ud = 25:25:125; % Discharge Voltage
P = 90:625:6250; % 100:100:500 % Watt
Loss = 4 ; % Wall Loss In Percent
Eff = 0.9 ; % Inonizaation Efficiency
nn = 1.2 * 10^19; % m^-3 (Atomic number density)
alpha = 0.9 ; %(Propellant conversion efficiency)
%
 ============================================================================
dm = sqrt(P'./ (1000 .*Ud)); % [m]
dmm = dm *1000; % [mm]
wmm = 0.242 * dmm; % [mm]
wm = wmm/1000; % [m]
mframgs = 0.003 .* wmm .* dmm; % [mg/s]
mfrakgs = 0.003 .* wm .* dm; % [kg/s]
figure,
plot(P,mframgs,'LineWidth',1);
title('Power Vs. Anode Flow Rate');
legend('V = 25', 'V = 50','V = 75', 'V = 100','V = 125');
xlabel('Power [W]');
ylabel('Anode Flow Rate [In mg/s]');
grid on;
figure,
plot(Ud,mframgs,'LineWidth',1);
title('Discharge Voltage Vs. Anode Flow Rate');
legend('P = 90', 'P = 715','P = 1340','P = 1965','P = 2590','P =
 3215','P = 3840','P = 4465','P = 5090','P = 5715');
xlabel('Discharge Voltage [In V]');
ylabel('Anode Flow Rate [In mg/s]');
grid on;
```

```
clear all;
clc;

% This code plots the Power Vs. Thrust and Discharge Voltage Vs.
 Thrust.

Ud = 25:25:125; % Discharge Voltage
P = 90:625:6250; % 100:100:500 % Watt
Loss = 4 ; % Wall Loss In Percent
Eff = 0.9 ; % Inonizaation Efficiency
nn = 1.2 * 10^19; % m^-3 (Atomic number density)
alpha = 0.9 ; %(Propellant conversion efficiency)
%
 ================================================================================
dm = sqrt(P'./ (1000 .*Ud)); % [m]
dmm = dm *1000; % [mm]
wmm = 0.242 * dmm; % [mm]
wm = wmm/1000; % [m]
mframgs = 0.003 .* wmm .* dmm; % [mg/s]
mfrakgs = 0.003 .* wm .* dm; % [kg/s]
Tn = 892.7 .* mfrakgs .* sqrt(Ud); % Thrust in Newtons
Tmn = Tn.*1000; % Thrust in mN
figure,
plot(P,Tn,'LineWidth',1);
title('Power Vs. Thrust');
legend('V = 25', 'V = 50','V = 75', 'V = 100','V = 125');
xlabel('Power [W]');
ylabel('Thrust [In N]');
grid on;
figure,
plot(Ud,Tn,'LineWidth',1);
title('Discharge Voltage Vs. Thrust');
legend('P = 90', 'P = 715','P = 1340','P = 1965','P = 2590','P =
 3215','P = 3840','P = 4465','P = 5090','P = 5715');
xlabel('Discharge Voltage [In V]');
ylabel('Thrust [In N]');
grid on;
```

```
clear all;
clc;

% This code plots the Power Vs. Channel Length and Discharge Voltage
 Vs.
% Channel Length.

Ud = 25:25:125; % Discharge Voltage
P = 90:625:6250; % 100:100:500 % Watt
Loss = 4 ; % Wall Loss In Percent
Eff = 0.9 ; % Inonizaation Efficiency
nn = 1.2 * 10^19; % m^-3 (Atomic number density)
alpha = 0.9 ; %(Propellant conversion efficiency)
cp1 = 1.2*10^6;
Ct2 = 0.109;
%
 ================================================================================
dm = sqrt(P'./ (1000 .*Ud)); % [m]
dmm = dm *1000; % [mm]
wmm = 0.242 * dmm; % [mm]
wm = wmm/1000; % [m]
mframgs = 0.003 .* wmm .* dmm; % [mg/s]
mfrakgs = 0.003 .* wm .* dm; % [kg/s]
Tn = 892.7 .* mfrakgs .* sqrt(Ud); % Thrust in Newtons
wd = P./cp1;
Lm = (Ct2.*sqrt(Ud').*wd)./(Tn');
Lmm = Lm.*1000;
figure,
plot(P,Lmm,'LineWidth',1);
title('Power Vs. Channel Length');
legend('V = 25', 'V = 50','V = 75', 'V = 100','V = 125');
xlabel('Power [W]');
ylabel('Channel Length [In mm]');
grid on;
figure,
plot(Ud,Lmm,'LineWidth',1);
title('Discharge Voltage Vs. Channel Length');
xlabel('Discharge Voltage [In V]');
ylabel('Channel Length [In mm]');
grid on;
```

```
clear all;
clc;

% This code plots the Power Vs. Specific Impulse and Discharge Voltage
 Vs.
% Specific Impulse.

Ud = 25:25:125; % Discharge Voltage
P = 90:625:6250; % 100:100:500 % Watt
Loss = 4 ; % Wall Loss In Percent
Eff = 0.9 ; % Inonizaation Efficiency
nn = 1.2 * 10^19; % m^-3 (Atomic number density)
alpha = 0.9 ; %(Propellant conversion efficiency)
cp1 = 1.2*10^6;
Ct2 = 0.109;
%
 ================================================================================
dm = sqrt(P'./ (1000 .*Ud)); % [m]
dmm = dm *1000; % [mm]
wmm = 0.242 * dmm; % [mm]
wm = wmm/1000; % [m]
mframgs = 0.003 .* wmm .* dmm; % [mg/s]
mfrakgs = 0.003 .* wm .* dm; % [kg/s]
Tn = 892.7 .* mfrakgs .* sqrt(Ud); % Thrust in Newtons
wd = P./cp1;
Lm = (Ct2.*sqrt(Ud').*wd)./(Tn');
Lmm = Lm.*1000;
g = 9.81; % Gravity
Isp = Tn./(mfrakgs.*g); % Specific Impulse
figure,
plot(P,Isp,'LineWidth',1);
title('Power Vs. Specific Impulse');
legend('V = 25', 'V = 50','V = 75', 'V = 100','V = 125');
xlabel('Power [W]');
ylabel('Specific Impulse [In S]');
grid on;
figure,
plot(Ud,Isp,'LineWidth',1);
title('Discharge Voltage Vs. Specific Impulse');
xlabel('Discharge Voltage [In V]');
ylabel('Specific Impulse [In S]');
grid on;
```

Appendix B – NAGA-II Algorithm MATLAB Code

```
clc;
clear;
close all;

% Problem Definition

CostFunction=@(x) MOP4(x);      % Cost Function

nVar=3;             % Number of Decision Variables

VarSize=[1 nVar];   % Size of Decision Variables Matrix

VarMin=-5;          % Lower Bound of Variables
VarMax= 5;          % Upper Bound of Variables

% Number of Objective Functions
nObj=numel(CostFunction(unifrnd(VarMin,VarMax,VarSize)));


% NSGA-II Parameters

MaxIt=100;      % Maximum Number of Iterations

nPop=50;        % Population Size

pCrossover=0.7;                         % Crossover Percentage
nCrossover=2*round(pCrossover*nPop/2);  % Number of Parnets
 (Offsprings)

pMutation=0.4;                          % Mutation Percentage
nMutation=round(pMutation*nPop);        % Number of Mutants

mu=0.02;                    % Mutation Rate

sigma=0.1*(VarMax-VarMin);  % Mutation Step Size


% Initialization

empty_individual.Position=[];
empty_individual.Cost=[];
empty_individual.Rank=[];
empty_individual.DominationSet=[];
empty_individual.DominatedCount=[];
empty_individual.CrowdingDistance=[];

pop=repmat(empty_individual,nPop,1);

for i=1:nPop

    pop(i).Position=unifrnd(VarMin,VarMax,VarSize);
```

```
    pop(i).Cost=CostFunction(pop(i).Position);

end

% Non-Dominated Sorting
[pop, F]=NonDominatedSorting(pop);

% Calculate Crowding Distance
pop=CalcCrowdingDistance(pop,F);

% Sort Population
[pop, F]=SortPopulation(pop);


% NSGA-II Main Loop

for it=1:MaxIt

    % Crossover
    popc=repmat(empty_individual,nCrossover/2,2);
    for k=1:nCrossover/2

        i1=randi([1 nPop]);
        p1=pop(i1);

        i2=randi([1 nPop]);
        p2=pop(i2);

        [popc(k,1).Position,
 popc(k,2).Position]=Crossover(p1.Position,p2.Position);

        popc(k,1).Cost=CostFunction(popc(k,1).Position);
        popc(k,2).Cost=CostFunction(popc(k,2).Position);

    end
    popc=popc(:);

    % Mutation
    popm=repmat(empty_individual,nMutation,1);
    for k=1:nMutation

        i=randi([1 nPop]);
        p=pop(i);

        popm(k).Position=Mutate(p.Position,mu,sigma);

        popm(k).Cost=CostFunction(popm(k).Position);

    end

    % Merge
    pop=[pop
         popc
         popm];
```

```
    % Non-Dominated Sorting
    [pop, F]=NonDominatedSorting(pop);

    % Calculate Crowding Distance
    pop=CalcCrowdingDistance(pop,F);

    % Sort Population
    pop=SortPopulation(pop);

    % Truncate
    pop=pop(1:nPop);

    % Non-Dominated Sorting
    [pop, F]=NonDominatedSorting(pop);

    % Calculate Crowding Distance
    pop=CalcCrowdingDistance(pop,F);

    % Sort Population
    [pop, F]=SortPopulation(pop);

    % Store F1
    F1=pop(F{1});

    % Show Iteration Information
    disp(['Iteration ' num2str(it) ': Number of F1 Members = '
 num2str(numel(F1))]);

    % Plot F1 Costs
    figure(1);
    PlotCosts(F1);
    pause(0.01);

end
```

```
Iteration 1: Number of F1 Members = 5
Iteration 2: Number of F1 Members = 8
Iteration 3: Number of F1 Members = 11
Iteration 4: Number of F1 Members = 19
Iteration 5: Number of F1 Members = 28
Iteration 6: Number of F1 Members = 37
Iteration 7: Number of F1 Members = 33
Iteration 8: Number of F1 Members = 42
Iteration 9: Number of F1 Members = 50
Iteration 10: Number of F1 Members = 50
Iteration 11: Number of F1 Members = 50
Iteration 12: Number of F1 Members = 50
Iteration 13: Number of F1 Members = 50
Iteration 14: Number of F1 Members = 50
Iteration 15: Number of F1 Members = 50
Iteration 16: Number of F1 Members = 50
Iteration 17: Number of F1 Members = 50
Iteration 18: Number of F1 Members = 50
```

```
function pop=CalcCrowdingDistance(pop,F)

    nF=numel(F);

    for k=1:nF

        Costs=[pop(F{k}).Cost];

        nObj=size(Costs,1);

        n=numel(F{k});

        d=zeros(n,nObj);

        for j=1:nObj

            [cj, so]=sort(Costs(j,:));

            d(so(1),j)=inf;

            for i=2:n-1

                d(so(i),j)=abs(cj(i+1)-cj(i-1))/abs(cj(1)-cj(end));

            end

            d(so(end),j)=inf;

        end


        for i=1:n

            pop(F{k}(i)).CrowdingDistance=sum(d(i,:));

        end

    end

end


function [y1, y2]=Crossover(x1,x2)

    alpha=rand(size(x1));

    y1=alpha.*x1+(1-alpha).*x2;
    y2=alpha.*x2+(1-alpha).*x1;

end
```

```
function b=Dominates(x,y)

    if isstruct(x)
        x=x.Cost;
    end

    if isstruct(y)
        y=y.Cost;
    end

    b=all(x<=y) && any(x<y);

end
function y=Mutate(x,mu,sigma)

    nVar=numel(x);

    nMu=ceil(mu*nVar);

    j=randsample(nVar,nMu);
    if numel(sigma)>1
        sigma = sigma(j);
    end

    y=x;

    y(j)=x(j)+sigma.*randn(size(j));

end
```

```
function [pop, F]=NonDominatedSorting(pop)

    nPop=numel(pop);

    for i=1:nPop
        pop(i).DominationSet=[];
        pop(i).DominatedCount=0;
    end

    F{1}=[];

    for i=1:nPop
        for j=i+1:nPop
            p=pop(i);
            q=pop(j);

            if Dominates(p,q)
                p.DominationSet=[p.DominationSet j];
                q.DominatedCount=q.DominatedCount+1;
            end

            if Dominates(q.Cost,p.Cost)
                q.DominationSet=[q.DominationSet i];
                p.DominatedCount=p.DominatedCount+1;
            end

            pop(i)=p;
            pop(j)=q;
        end

        if pop(i).DominatedCount==0
            F{1}=[F{1} i];
            pop(i).Rank=1;
        end
    end

    k=1;

    while true

        Q=[];

        for i=F{k}
            p=pop(i);

            for j=p.DominationSet
                q=pop(j);

                q.DominatedCount=q.DominatedCount-1;

                if q.DominatedCount==0
                    Q=[Q j];
```

```
                    q.Rank=k+1;
                end

                pop(j)=q;
            end
        end

        if isempty(Q)
            break;
        end

        F{k+1}=Q;

        k=k+1;

    end


end

function [pop, F]=SortPopulation(pop)

    % Sort Based on Crowding Distance
    [~, CDSO]=sort([pop.CrowdingDistance],'descend');
    pop=pop(CDSO);

    % Sort Based on Rank
    [~, RSO]=sort([pop.Rank]);
    pop=pop(RSO);

    % Update Fronts
    Ranks=[pop.Rank];
    MaxRank=max(Ranks);
    F=cell(MaxRank,1);
    for r=1:MaxRank
        F{r}=find(Ranks==r);
    end

end
```